

Single bacterial resolvases first exploit, then constrain intrinsic dynamics of the Holliday junction to direct recombination

Sujay Ray^{ID†}, Nibedita Pal^{ID†} and Nils G. Walter^{ID*}

Single Molecule Analysis Group, Department of Chemistry, University of Michigan Ann Arbor, MI 48109, USA

Received April 29, 2020; Revised January 30, 2021; Editorial Decision February 02, 2021; Accepted February 06, 2021

ABSTRACT

Homologous recombination forms and resolves an entangled DNA Holliday Junction (HJ) crucial for achieving genetic reshuffling and genome repair. To maintain genomic integrity, specialized resolvase enzymes cleave the entangled DNA into two discrete DNA molecules. However, it is unclear how two similar stacking isomers are distinguished, and how a cognate sequence is found and recognized to achieve accurate recombination. We here use single-molecule fluorescence observation and cluster analysis to examine how prototypic bacterial resolvase RuvC singles out two of the four HJ strands and achieves sequence-specific cleavage. We find that RuvC first exploits, then constrains the dynamics of intrinsic HJ isomer exchange at a sampled branch position to direct cleavage toward the catalytically competent HJ conformation and sequence, thus controlling recombination output at minimal energetic cost. Our model of rapid DNA scanning followed by ‘snap-locking’ of a cognate sequence is strikingly consistent with the conformational proofreading of other DNA-modifying enzymes.

INTRODUCTION

The Holliday Junction (HJ) is a topologically constrained four-way DNA junction formed during homologous recombination, an evolutionarily conserved process widely used across cellular life for reshuffling genetic information, rescuing broken replication forks, and repairing DNA strand breaks (1–5). At the penultimate stage of homologous recombination, resolving the HJ is required to restore the entangled four-way DNA junction into two discrete DNA molecules. Accurate resolution of the two appropriate edges of the HJ is crucial for the desired crossover or

non-crossover recombination output (Supplementary Figure S1a). In Gram-negative bacteria such as *Escherichia coli*, HJ resolution is carried out by endonuclease RuvC, a well-studied, prototypical resolvase with extremely high topology and sequence specificity (6–8). To achieve site-specific resolution, the HJ needs to be correctly positioned at the catalytic site (Supplementary Figure S1b) through branch migration of the junction, which occurs either spontaneously or catalyzed by the RuvAB complex (9,10). A homodimer of RuvC can bind an HJ independently of RuvAB (11–13) to introduce two interdependent nicks via a two-Mg²⁺ catalytic mechanism (7,14,15).

Substrate specificity is an important feature shared among HJ resolvases across organisms (16). Numerous *in vitro* studies with synthetic DNA strands have shown that the eventual resolution of HJs by RuvC involves both structure- and sequence-specific contacts. Even though intrinsic conformational exchange between two alternatively stacked, X-shaped conformational isomers (*iso-I* and *iso-II*) (17–20) repeatedly modulates the sequences on the continuous and bent DNA strands, RuvC recognizes an HJ structurally but independently of sequence; only junction cleavage is strictly sequence-specific. These observations suggest that screening of the consensus sequence by RuvC may involve sampling dynamic signatures among rapidly exchanging HJ isomers. Interestingly, in a recent study Zhou *et al.* demonstrated that binding of RuvC to a HJ does not arrest these intrinsic fluctuations (21). In fact, the bound RuvC disengages some of its multivalent contacts to allow the HJ to undergo nearly unimpeded conformer exchange as well as branch migration, by partially dissociating from the HJ (PD ‘state’ or complex) (21). This important insight was achieved upon suppressing cleavage by using Ca²⁺ instead of Mg²⁺ and by not including the cognate cleavage sequence, both strict requirements for RuvC mediated cleavage. Therefore, it has remained unclear how RuvC achieves its remarkable cleavage specificity for the cognate 5'-ATT[↓]X-3' sequence (X = G/C; ↓ = cleavage site) to en-

*To whom correspondence should be addressed. Tel: +1 734 615 2060; Fax: +1 734 615 5524; Email: nwalter@umich.edu

†The authors wish it to be known that, in their opinion, the first two authors should be regarded as Joint First Authors.

Present addresses:

Sujay Ray, Wyss Institute for Biologically Inspired Engineering at Harvard University, Boston, MA 02115, USA.

Nibedita Pal, Indian Institute of Science Education and Research (IISER) Tirupati, Tirupati 517507, Andhra Pradesh, India.

sure proper control over chromosome segregation (6,8,22–24). Prior investigations using bulk fluorescence techniques, X-ray crystallography, electrophoretic mobility shift assays, and computational simulations showed that RuvC distorts the junction at the crossover point (Supplementary Figure S1b), possibly including protein-assisted base flipping, and resolves the junction by introducing two symmetric nicks on the continuous strands 3' of the thymine residues (11,12,14,15,25). However, since the HJ undergoes rapid conformational fluctuation between two isomers in the presence of both divalent metal ions and resolvase, an important conundrum is the dynamic mechanism by which RuvC discriminates between the two similar junction topologies of *iso-I* and *iso-II* with differing junction sequences to choose a catalytically competent conformation.

Here, we leverage single-molecule Förster resonance energy transfer (smFRET) to investigate the dynamic interaction of *E. coli* RuvC with an HJ that can be cleaved and thus leads to sequence-specific junction resolution. Instead of focusing on the previously characterized binding properties of RuvC to the unimpeded HJ dynamics (21), our work aims to dissect how the HJ-RuvC complex advances to cleavage upon recognition of a cleavage-active sequence. First, we confirm that the resolvase binds both cleavage-incompetent (*iso-I*) and –competent (*iso-II*) conformations, wherein the cognate sequences reside on the two bent and continuous (i.e. non-crossover) strands, respectively (Figure 1A). Consistent with the report by Zhou *et al.* (21) we observe that RuvC interferes little with the conformational isomerization of the HJ, corroborating the formation of a PD complex by the enzyme.

Second, we discover that RuvC in fact takes advantage of these intrinsic HJ conformational and branch migration dynamics to find and then kinetically trap the catalytically active conformation through transition from fluctuations between *iso-I*, *iso-II* and a partially open state to fluctuations between only *iso-II* and the partially open state. These dynamic transitions are observed exclusively when RuvC acts on its cognate cleavage sequence in the presence of Mg²⁺. Based on these findings, we propose an expanded model wherein RuvC exploits the inherent HJ dynamics until the cognate sequence enters its active site through branch migration, in turn inducing a snap-lock conformational switch of the DNA-protein complex that helps RuvC achieve its high sequence specificity at low energetic cost. Our findings underscore the role of the cognate sequence in inducing the protein to lock the HJ into a cleavage competent conformation.

MATERIALS AND METHODS

HJ preparation

HPLC purified oligonucleotides of the following sequences (see Supplementary Table S1) were bought from Integrated DNA Technologies (IDT) and were used for single-molecule and bulk experiments without further purification. HJ_{Xh}^R junctions were prepared by mixing the B and H strands and X and R strands separately at 2:1 ratios in 20 mM Tris-HCl, pH 8.0, and 500 mM NaCl, annealed by heating to 70°C and slow (~0.5°C/min) cooling to 30°C. The concentrations of strand B, H, X, and R were 2, 1, 2 and

1 μM respectively. At 30°C, these two annealing mixtures were combined and slowly (~0.5°C/min) cooled to 4°C. Assembled junctions were stored at 4°C until further use. A simple simulation of complex formation using the software package NUPACK (<http://www.nupack.org/>) is summarized in Supplementary Table S3 to emphasize formation of major complexes.

Protein Purification

Recombinant *E. coli* RuvC was purchased from Abcam (ab63828, >90 % SDS-PAGE pure) and used for all experiments. All concentrations used here refer to the monomer, which forms homo-dimers.

smFRET assay

Cleaned optical quartz slides and glass coverslips were used to prepare imaging chambers. Surfaces were passivated with a mixture of polyethylene-glycol (PEG) and biotinylated polyethylene-glycol (Laysan Bio.) to prevent nonspecific surface absorption of the biomolecules. The details of surface passivation and construction of microfluidic channel are described elsewhere (26,27). Additionally, the chambers were incubated with 10 mg/ml BSA to further reduce nonspecific surface binding of RuvC by coating any sticky patches on the PEG-surface. Fluorescently labeled HJs were immobilized on the biotin-PEG surface through biotin-streptavidin interactions. 100–200 pM biotinylated HJ prepared in 20 mM Tris-HCl, pH 8.0, without Mg²⁺ was added for surface immobilization. Excess HJs were washed away by injecting a wash buffer containing 20 mM Tris-HCl, pH 8.0, and 0.1 mg/ml BSA without the HJs. Titration experiments were performed in 20 mM Tris-HCl, pH 8.0, and at 5, 10 or 25 mM Mg²⁺. An oxygen scavenger system (OSS) comprised of 50 nM protocatechuate-3,4-dioxygenase (PCD), 5 mM protocatechuic acid (PCA), and 2 mM 6-hydroxy-2,5,7,8-tetramethylchroman-2-carboxylic acid (Trolox) was used to minimize both photobleaching and blinking of the fluorophores. 400 nM RuvC was added at the same ionic and pH conditions for protein binding and cleavage experiments. The smFRET experiments were carried out at room temperature unless otherwise mentioned.

smFRET data acquisition using TIRFM

Prism-based total internal reflection fluorescence microscopy (TIRFM) was used to acquire smFRET data as described (27,28). Briefly, a 532 nm green laser from Laser Quantum and a 638 nm red laser from Coherent were used to excite Cy3 and Cy5, respectively. Fluorescence was collected by using a 60× 1.2NA water immersion objective (Olympus UplanoApo). The fluorescence was divided into two channels (donor and acceptor) by using appropriate dichroic mirrors and projected onto two Hamamatsu Flash4.0-V3 sCMOS cameras. The data collection was performed using a LabView based data acquisition code. The typical data collection time was ~30–40 s at 40 ms time resolution. Typically, the OSS was pre-incubated for 5 min to remove molecular oxygen before data acquisition was started. 175–200 mW green laser power was used to elicit sufficient

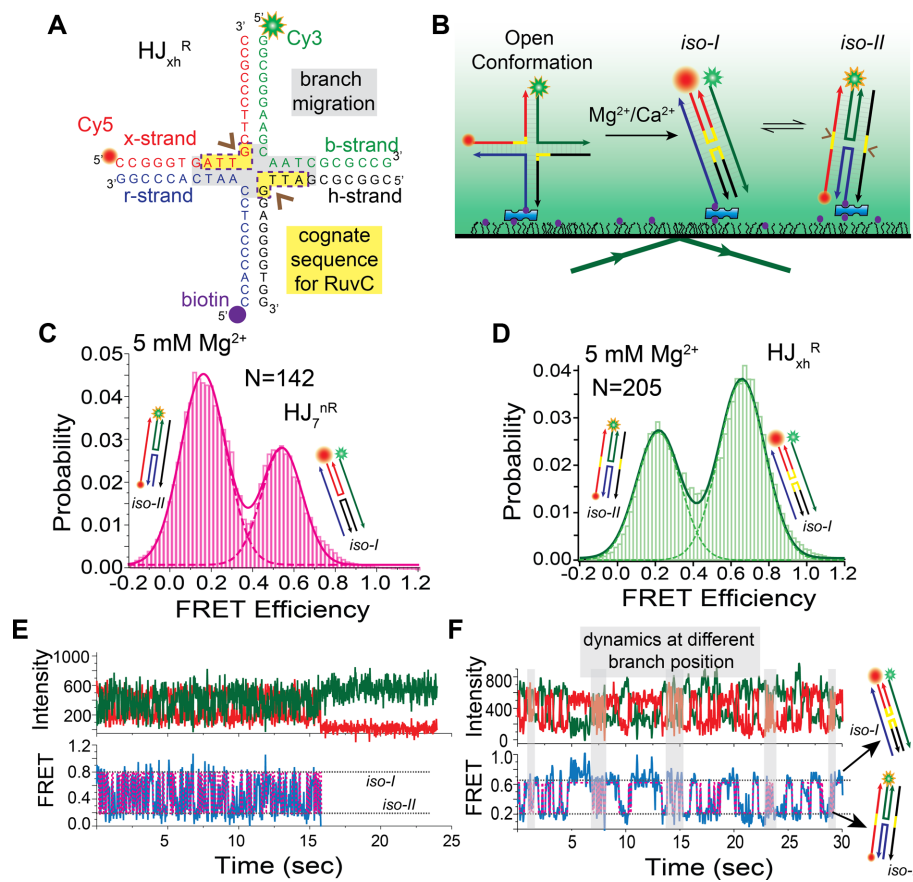


Figure 1. Holliday junction design to observe conformational dynamics by smFRET. **(A)** Schematic and sequence of the HJ_{xh}^R design. The nucleotides highlighted in yellow represent the cognate cleavage sequence for RuvC. The nucleotides highlighted in gray represent the region of the junction that can potentially branch migrate due to sequence homology. The brown arrows indicate the cleavage sites. The 5' ends of the r, x and b-strand are labeled with biotin, Cy5 and Cy3, respectively. **(B)** Schematic of our smFRET assay under TIRF illumination to monitor the dynamics of HJ_{xh}^R molecules. The HJ transitions between two isomeric states *iso-I* and *iso-II*. The cognate sequences are shown in yellow in the bent, cleavage-incompetent *iso-I* and continuous, cleavage-competent *iso-II* strands. **(C)** Single molecule FRET probability distribution of HJ₇^{nR} in presence of 5 mM Mg²⁺. **(D)** Single molecule FRET histogram of HJ_{xh}^R construct in presence of 5 mM Mg²⁺. **(E)** Representative single-molecule time trajectory showing donor (green) and acceptor (red) intensity in the top panel, FRET (blue) and HMM fitted to the data (magenta) in the bottom panel of HJ₇^{nR}. **(F)** Representative single-molecule time trajectory showing donor (green) and acceptor (red) intensity in the top panel, FRET (blue) and HMM fitted to the data (magenta) in the bottom panel of HJ_{xh}^R. Fast transitions highlighted in gray are attributed to conformer exchange at a different branchpoint position. Representative cartoons indicate the conformational states associated with particular FRET values.

emission photons at this high time resolution. At the end of data collection, Cy5 was directly excited using the 638 nm laser (~100 mW) to confirm the presence of the Cy5 dye.

Analysis of smFRET data

A MATLAB based analysis script was used to generate intensity time traces from the recorded movies for further detailed kinetic analysis. Dwell times in different FRET states (E_{FRET}) were extracted from smFRET time traces by using hidden Markov models (HMM) fitted within Qub (29). The HMM fitted curves were used further to construct FRET probability distributions and Transition Occupancy Density Plots (TODPs) using home-built MATLAB codes (29). OriginPro was used for multi-peak fitting of the FRET probability distributions, which represent normalized frame-by-frame FRET values of all FRET trajectories in a given dataset. By contrast, TODPs capture the interconversion between pairs of FRET states as a two-

dimensional heat map of final versus initial FRET state, weighted by the fraction of molecules displaying that particular transition. Highly reversible conformational transitions between distinguishable states appear as peak pairs that are symmetric relative to the main diagonal, whereas populations on the diagonal represent molecules that do not undergo any conformational transitions within the observation time window (29). To calculate transition rate constants between distinguished states, all dwell times in a particular FRET state are extracted across trajectories contributing to that population in the TODP by pooling transition times from a user specified region (see Supplementary Figure S10) using a home-built MATLAB code. This approach separates the dwell times of different pathways based on the initial and final FRET states visited. Thus, the extracted rate constant for a particular transition is not contaminated by other transitions. A cumulative frequency histogram of these dwells times is then fitted using OriginPro with the single-exponential function

$y(t) = y_0 + A(1 - e^{kt})$, where y_0 is the offset (if any), A is the amplitude and k is the rate constant. Cumulative frequency representations of dwell times are particularly useful for estimating the number of possible rate constants present in the system, which in turn represents the number of interconverting species (30–32). Of note, accurate determination of rate constants from non-cumulative frequency histograms requires large datasets since for smaller datasets it becomes sensitive to the bin size. By contrast, in our cumulative frequency distributions each data point is given equal weight, which makes the analysis less susceptible to binning artefacts.

Gel based cleavage assays

We titrated different concentrations of RuvC into pre-formed HJ in cleavage buffer (20 mM Tris-HCl, pH-8, 20 mM NaCl, 1 mM EDTA, 1 mM DTT, 0.1 mg/ml BSA, 10 mM or 5 mM MgCl₂ or CaCl₂) at 37°C or RT as specified. The reaction was quenched by adding EDTA and gel loading buffer, then denatured by heating at 90°C for 10 min. The samples were analyzed by 15% denaturing urea-polyacrylamide gel electrophoresis in standard 1x TAE buffer (gel loading buffer (1×): 1× TAE buffer, 45% formamide, 0.005% Bromophenol Blue) run at 25 W constant power for ~3 h. Each of the four strands of HJ_{xh}^R are 20 nt long. If the junction is resolved by RuvC, 10 nt long pieces will be generated. Our analysis of HJ_{xh}^R cleavage showed the intact 20-nt band and the 10 nt cleavage product (Figure 2A, Supplementary Figure S6). To rule out non-specific degradation of the DNA, we also scanned the gel for the Cy3 dye, which by design represents a non-cleavable strand. As expected, the Cy3 scan shows only one band, matching the 20-nt length. A cleavage reaction isotherm curve fit using a Michaelis-Menten equation resulted in a half-titration RuvC_{1/2} value of ~66 nM.

To determine kinetic parameters, we performed a time course of the cleavage reaction. The reaction under the experimental conditions of 10 mM Mg²⁺ at 37°C, 5 mM Mg²⁺ at 37°C, 10 mM Mg²⁺ at room temperature (RT), 5 mM Mg²⁺ at RT, or 10 mM Ca²⁺ at 37°C was quenched at specific time points and loaded onto a denaturing gel as above. Quantification of the gel image yielded a cleavage reaction time course, the data of which were fitted with single-exponential functions ($y(t) = y_0 + A(1 - e^{kt})$) to extract rate constants. We found that the 10 mM Mg²⁺ at 37°C condition yielded the most significant cleavage, while 5 mM Mg²⁺ at RT and 10 mM Ca²⁺ at 37°C showed very little to no cleavage, suggesting that the reaction temperature, salt concentration, and counter ion type all have significant effects on RuvC-mediated HJ cleavage.

Single molecule cleavage assay

The cleavage sites in HJ_{xh}^R are designed such that the Cy5 labeled DNA strand will remain bound to the surface via its hybridization to the biotinylated r-strand, while the Cy3 labeled b strand will leave the surface upon cleavage. The microscope slide was imaged in the microscope at the beginning of the experiment. 400 nM RuvC was then introduced to the sample chamber and the slide kept at 37°C for 1 h

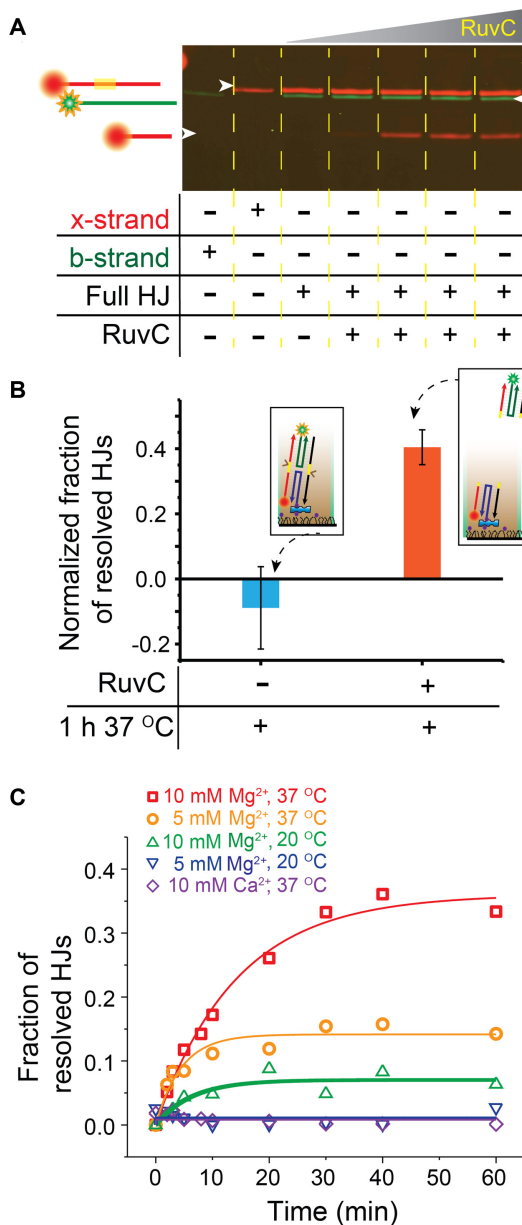


Figure 2. Holliday junction cleavage by RuvC. **(A)** Superimposed Cy3 (green) and Cy5 (red) scans of a denaturing urea-polyacrylamide gel showing RuvC-mediated cleavage of HJ_{xh}^R in the presence of varying concentrations of RuvC (0, 50, 100, 200 and 400 nM respectively from lanes 3–7). The top bands represent the full-length 20-nt-long DNA; the bottom bands are the cleaved 10-nt-long DNA product. The schematics on the right-hand side represent the relative length of DNA corresponding to each band. The Cy3-labeled b strand is not cleaved due to the absence of a cleavage sequence. **(B)** Quantification of cleavage using a single molecule assay. Normalized ratios of number of colocalized Cy3–Cy5 spots and number of all Cy5 spots before and after cleavage were calculated to estimate the fraction of cleaved HJs regardless of slide to slide variation in the number of initial HJ molecules. The fraction of resolved HJs are plotted for the presence and absence of RuvC. Without RuvC, this ratio remains close to zero. In the presence of 10 mM Mg²⁺ and 400 nM RuvC incubated at 37°C for 1 h, this ratio becomes 0.40±0.05, representing RuvC-mediated cleavage. The inset shows a schematic of the experiment before and after cleavage in the presence of RuvC. **(C)** Quantitative analysis of a time course of RuvC-mediated cleavage of HJ_{xh}^R under varying conditions as indicated, at 400 nM RuvC. Saturation curves are fit to the data. As expected, the fraction of HJ_{xh}^R molecules cleaved by RuvC decreases with decreasing temperature and decreasing Mg²⁺ concentration.

for the cleavage reaction to occur. After 1 h, the microscope slide was imaged under the same imaging conditions as before. As a control we performed the same experiment where no RuvC was introduced to the slide. We calculated the ratio of the number of colocalized Cy3/Cy5 spots and the number of all Cy5 spots as a measure of how many HJs are intact in our imaging conditions at time zero and after the cleavage reaction. The change is normalized by the initial ratio to compensate for slide-to-slide variability, as follows:

Fraction of cleaved HJ

$$= \frac{\left(\frac{\# \text{ Colocalized Spots}}{\# \text{ All Cy5 Spots}}\right)_{t_0} - \left(\frac{\# \text{ Colocalized Spots}}{\# \text{ All Cy5 Spots}}\right)_{t_T}}{\left(\frac{\# \text{ Colocalized Spots}}{\# \text{ All Cy5 Spots}}\right)_{t_0}}$$

While in the presence of RuvC we found evidence for ~40% cleavage, in the control measurements we saw little to no change in the ratios. A slightly negative value for the fraction in the control measurement is found as the change in the number of molecules and the number of colocalizations is extremely small. As a result, we also have a high error bar. In light of this error, we conclude that this small negative value is well within the range of observational error of the experiment and may arise from loss of a few Cy3 molecules due to excess slight photobleaching or degradation of the DNA.

Fano factor calculation

The Fano factor is defined as, $= \frac{\sigma_T^2}{\mu_T}$, where σ_T^2 is the variance and μ_T is the mean of a random process in some time window ' T '. The Fano factor is a measure of the reliability with which the random variable could be estimated from a time window that on average contains several random events. For a Poisson process, the theoretical Fano factor is exactly one. However, due to experimental variability in the event sequence for an experimental Poisson process, the Fano factor asymptotically follows a gamma distribution with dependence on the number of observations of event counts (in our case, FRET transitions) (33). As a rule of thumb, any variability in the event or spike train of a Poisson process is considered to be within error if the Fano factor falls within a 95% confidence window around the expected value of one (34). Here, we calculated Fano factors for datasets measured at 5 mM Mg²⁺ only, and the (*iso-I*↔*O_P*)_R and (*iso-II*↔*O_P*)_R segments of the mixed R-cluster traces over time windows of 1.25, 2.5, 4, 5, 6, 8 and 10 s. We observed that the 5 mM Mg²⁺ only and (*iso-I*↔*O_P*)_R segment data deviated from a pure Poisson process, whereas the (*iso-II*↔*O_P*)_R segments displayed Poisson process behavior regardless of the time window.

Single molecule cluster analysis

To identify and visualize the various behavioral patterns in the smFRET trace data, single molecule cluster analysis (SiMCAn) was performed in MATLAB as described in detail elsewhere (35,36). Briefly, first-round clustering to identify common patterns of trace behavior was performed as follows: The SiMCAn FRET_processing.m script was used

to reassign the HMM-idealized FRET state values for each trace into 10 evenly spaced bins (centered at 0.05, 0.15, 0.25, ..., 0.95). Re-binned data files from all conditions were analyzed using SiMCAn Process_HMM_data.m file. The number of dynamic clusters (4) was chosen empirically to maximize the inter-cluster and minimize the intra-cluster differences and a hierarchical cluster tree was generated. Additional output plots for all identified dynamic clusters were generated using the same MATLAB script. Further segmentation of the 'mixed' traces so identified into early and late phases considered the trace from five seconds prior to the transition from pairwise *iso-I*_R↔*O_P*_R to pairwise *iso-II*_R↔*O_P*_R dynamics, whereas the late phase considers the trace from the transition point to five second after.

Description of each cluster

To elaborate, clusters S1, S2 and S3 in Supplementary Figure S10 represent buffer-only behaviors and R (purple) represents RuvC-HJ complex behavior (as mentioned in the diagram). The red, cyan, green and purple colors assigned to S1, S2, S3 and R, respectively, do not carry any merits other than visual aid. There are only subtle differences between the FRET states of the salt-like clusters S1, S2 and S3. In our experiments, the three S-clusters may represent HJs at different branch migration positions of the central homology region. Regardless, the main purpose of utilizing SiMCAn is to help decouple the dynamics of HJ-only molecules from those of HJ-RuvC complexes. Accordingly, we assigned clusters S1–S3 as RuvC-unbound populations based on the observation that these clusters contain molecules predominantly from conditions where either RuvC is absent or not cleavage active.

We further performed a second layer of SiMCAn analysis on cluster R, after segmenting its traces into early and late phases relative to the time of switching from the *iso-I*_R↔*O_P*_R↔*iso-II*_R dynamics to the pairwise *iso-II*_R↔*O_P*_R dynamics. Trace segments become grouped into four distinct clusters, Cl-1 and Cl-2 for the early phases and Cl-3 and Cl-4 for the late phases (Supplementary Figure S14a). The only differences between Cl-1 and Cl-2 on the one hand and Cl-3 and Cl-4 on the other are slight variations in FRET values, as could be caused by different HJ_{xh}^R branch positions or minor experimental variations. Thus Cl-1 and Cl-2 both are colored Red and Yellow, respectively. Similarly, Cl-3 and Cl-4 are colored Cyan and Blue, respectively. At this juncture, we wish to reiterate that these color codes do not carry any scientific value but serve as visual aids.

Cross-correlation analysis

The cross-correlation functions between the donor and acceptor fluorescence intensities were calculated for HJs showing a transition from early phase to late phase using the following equation:

$$C_{cross}(t) = \frac{\langle \delta I_D(0) \delta I_A(t) \rangle}{\langle \delta I_D(0) \delta I_A(0) \rangle}, \text{ where } \delta I(t) = I(t) - \langle I(t) \rangle$$

The average cross-correlations for early and late phases were calculated separately and fitted with double-exponential functions. The cross-correlation analysis for

$\text{HJ}_{\text{xh}}^{\text{R}}$ showed an overall slower dynamics in the late phase compared to the early phase.

RESULTS

Branch migration occurs in a HJ with cognate cleavage sequence

Although the initial recognition of a HJ by RuvC is independent of the junction sequence, we hypothesized that differences in HJ conformational dynamics may be exploited by the resolvase as a cue to distinguish an HJ with cognate sequence from one without. As central homology is an additional requirement for efficient HJ cleavage by RuvC, we chose an HJ sequence that comprises the resolvase's cognate sequence within 5 base pairs of sequence homology and positioned for optimal cleavage activity (22) across the junction on the x- and h-strands ($\text{HJ}_{\text{xh}}^{\text{R}}$, Resolvable, Figure 1A). As a control, we selected a previously particularly well-studied HJ that contains neither the cleavable cognate sequence nor the central homology and hence is neither resolvable by RuvC (HJ_7^{nR} , non-Resolvable) nor allows for branch migration (19,21) (i.e. is ‘immobile’; see Supplementary Table S1 for the DNA sequences). Cyanine-3 (Cy3, donor) and Cyanine-5 (Cy5, acceptor) dyes on two arms of the HJ allow us to monitor the conformational dynamics using total internal reflection fluorescence (TIRF) based smFRET (Figure 1B), as exploited for other HJs (19,20,37–39) (Supplementary Figure S2). First, we measured the conformational dynamics of single $\text{HJ}_{\text{xh}}^{\text{R}}$ molecules under different divalent metal ion concentrations (without RuvC present). Consistent with previous reports on HJ dynamics (19,20,37–39), in the presence of either Mg^{2+} or Ca^{2+} $\text{HJ}_{\text{xh}}^{\text{R}}$ undergoes fast dynamic transitions between the two stacked isomeric conformers (19,20,37–39) *iso-I* and *iso-II* of high ($E_{\text{FRET}} = 0.65 \pm 0.12$) and low ($E_{\text{FRET}} = 0.21 \pm 0.11$) FRET efficiency, respectively (Figure 1C–F, and Supplementary Figure S2). The interconversion rate constants of $k_{I \rightarrow II} = 2.8 \pm 0.3 \text{ s}^{-1}$ and $k_{II \rightarrow I} = 4.0 \pm 0.4 \text{ s}^{-1}$ at 5 mM Mg^{2+} decrease gradually with increasing Mg^{2+} concentration (Supplementary Table S2, Figure S3). When Mg^{2+} was replaced with Ca^{2+} , only slightly slower kinetics were observed, indicating that $\text{HJ}_{\text{xh}}^{\text{R}}$ shows similar two-state isomerization dynamics in Mg^{2+} or Ca^{2+} as other HJs (Supplementary Figure S4) (19,20,37–39), with a slight (60%:40%) *iso-I:iso-II* bias dictated largely by the junction sequence (37,40).

Notably, variations in the FRET dynamics of $\text{HJ}_{\text{xh}}^{\text{R}}$ over time were detected by visual inspection (Figure 1F). Importantly, while our migration-immobile control HJ_7^{nR} shows comparable counter-ion dependent dynamics (Figure 1C, E) and interconversion rate constants (Supplementary Figure S5) with a 35%:65% *iso-I* ($E_{\text{FRET}} = 0.54 \pm 0.08$):*iso-II* ($E_{\text{FRET}} = 0.17 \pm 0.09$) population ratio, similar to previous observations (19,21), it lacks the distinct regimes of slow and fast FRET transitions of $\text{HJ}_{\text{xh}}^{\text{R}}$. We therefore conclude that these distinct regimes likely reflect $\text{iso-I} \leftrightarrow \text{iso-II}$ isomer exchange after migration to different branch positions (Figure 1F). These rates were calculated as overall rate constants and do not reflect transitions at specific branch positions. Similar evidence for branch migration was observed previously for another HJ with central homology, albeit without

cleavable cognate sequence (21,37). We hypothesized that the ability of the cognate sequence to migrate to the junction may allow RuvC to position itself in ways that enable cleavage.

Specific conditions allow decoupling of HJ conformational dynamics from cleavage

Next, we tested the $\text{HJ}_{\text{xh}}^{\text{R}}$ cleavage activity of RuvC upon incubation for 1 h at 37°C in standard cleavage buffer (20 mM Tris-HCl, pH-8, 20 mM NaCl, 1 mM EDTA, 1 mM DTT, 0.1 mg/ml BSA, 10 mM MgCl₂) by monitoring the appearance of the shortened Cy5 labeled cleavage product using denaturing gel electrophoresis (Figure 2A). Under these conditions, increasing the RuvC concentration yielded an isotherm with a half-saturation value $K_{1/2}$ of ~66 nM RuvC monomer (Supplementary Figure S6). Using TIRF microscopy to reach single molecule sensitivity, we instead monitored the disappearance of no longer surface-coupled Cy3-labeled product spots (Figure 2B), confirming that RuvC resolves single $\text{HJ}_{\text{xh}}^{\text{R}}$ molecules at 37°C in standard cleavage buffer. As a measure of how many HJs remained uncleaved under our imaging conditions, we calculated and compared the ratios of the number of colocalized Cy3/Cy5 spots and the number of all Cy5 spots at time zero and after the cleavage reaction. The change was normalized by the initial ratio to compensate for slide-to-slide variability (Materials and Methods). While in the presence of RuvC we observed ~40% cleavage, in control measurements without the enzyme we saw no loss of surface-coupled $\text{HJ}_{\text{xh}}^{\text{R}}$ (Figure 2B). At a saturating concentration of 400 nM RuvC (chosen to be >5-fold the $K_{1/2}$), the cleavage rate constant observed upon addition of RuvC was measured as $1.58 \times 10^{-3} \text{ s}^{-1}$, consistent with previous studies (22), while the maximal cleavage fraction was ~36%. When Mg^{2+} was replaced with Ca^{2+} under otherwise identical conditions, we observed almost no cleavage (<1%) in our bulk assays (Figure 2C). However, RuvC binding remains similar under these conditions (Supplementary Figure S7). Reactions performed at room temperature (20°C) and/or in the presence of only 5 mM Mg^{2+} also showed significantly reduced cleavage (Figure 2C), as expected (41). Such decreases in both rate and saturation level when using a sub-optimal reaction temperature for an enzyme is quite typical and is often exploited when crystallizing thermophilic enzymes.

These observations provide an opportunity to decouple the impact of RuvC on $\text{HJ}_{\text{xh}}^{\text{R}}$ conformational dynamics from its cleavage of the HJ, by choosing smFRET conditions of 20°C in 5 mM Mg^{2+} where cleavage is ~35-fold less efficient than at the optimal 37°C in 10 mM Mg^{2+} (Figure 2C). That is, while our cleavage assays confirm that $\text{HJ}_{\text{xh}}^{\text{R}}$ is properly resolved by RuvC, our decoupled smFRET conditions provide us with an opportunity to characterize the HJ's conformational dynamics involved in the resolution without interference by cleavage.

RuvC stabilizes an open conformation specifically in $\text{HJ}_{\text{xh}}^{\text{R}}$ with Mg^{2+} present

Using our decoupled smFRET conditions in the presence of saturating (400 nM) RuvC, we observed that the dynamic

exchange between *iso-I* and *iso-II* for HJ_{xh}^R becomes more complex (compare Figure 3A and B); in particular, a new mid-FRET state appears ($E_{\text{FRET}} = 0.4 \pm 0.1$) that lies between the high-FRET *iso-I* ($E_{\text{FRET}} = 0.64 \pm 0.13$) and the low-FRET *iso-II* ($E_{\text{FRET}} = 0.17 \pm 0.1$). This state is similar to the planar open conformation of the HJ in the absence of divalent metal ions ($E_{\text{FRET}} = 0.37 \pm 0.12$; Supplementary Figure S8) (15,21). We henceforth term this new state the RuvC-induced ‘open’, or Op, conformation. Upon replacing Mg²⁺ with Ca²⁺, this Op state disappears, leaving only *iso-I* ($E_{\text{FRET}} = 0.68 \pm 0.09$) and *iso-II* ($E_{\text{FRET}} = 0.15 \pm 0.08$; Figure 3C, D), suggesting that Mg²⁺ plays a specific role in stabilizing the Op state in the presence of RuvC. To ask whether the Op state is related to HJ cleavage, we tested for it in the non-cleavable HJ₇^{nR} as well as in another well-studied HJ termed HJ₃^{nR} (see Supplementary Table S1 for DNA sequences). Notably, under decoupled smFRET conditions we do not observe the Op state for HJ₇^{nR} that does not have a cognate cleavage sequence (Supplementary Figure S9). However, we expect RuvC binding to remain unimpaired under these conditions since we found it to bind to similar HJs even at low (1 mM) Ca²⁺ concentration (tested for HJ_{xh}^R, Supplementary Figure S7). The finding that Op is observed only in the presence of RuvC, Mg²⁺ and the cleavable cognate sequences (as present only in HJ_{xh}^R), all of which are required for cleavage, suggests that this state is relevant for HJ resolution. In fact, visual inspection revealed that ~40% of smFRET trajectories for HJ_{xh}^R visit Op, while the remainder continues to show two-state behavior only, most likely due to a lack of cleavage active RuvC binding (22). Notably, a very similar fraction of HJ molecules (~37%) are cleaved under optimal conditions (Figure 2C). This correlation supports the notion that most RuvC-bound HJ molecules accessing the Op state under decoupled smFRET conditions are cleavage-enabled and are the ones resolved under optimal cleavage conditions.

RuvC-HJ_{xh}^R complexes stabilize a catalytically competent, migration-arrested conformation

The stabilization of the Op state observed only for a HJ with the cleavable cognate sequence in the presence of both RuvC and Mg²⁺ led us to hypothesize that this state is associated with the catalytically competent RuvC-HJ complex. In fact, we observed that a large majority (~78%) of the HJ_{xh}^R molecules that visit the Op state do so as a transitory step into another dynamic state (Supplementary Figure S17). This finding strongly suggests that the Op state serves as a (near-)obligatory intermediate between two extreme FRET states (i.e. between *iso-I* and *iso-II*), as previously observed for protein-free, migration-active HJs (37). For a deeper probing of the dynamic features associated with this RuvC-induced conformation, we subjected $N = 673$ Hidden Markov Model (HMM) idealized smFRET traces from our four experimental HJ_{xh}^R conditions to model-independent hierarchical Single Molecule Cluster Analysis (SiMCA) (35,36); Figure 3A–D): 5 mM Mg²⁺, 5 mM Mg²⁺ plus 400 nM RuvC, 5 mM Ca²⁺, and 5 mM Ca²⁺ plus 400 nM RuvC. Using a hierarchical cluster tree, we grouped traces with similar FRET states and kinetics into four clusters. We observed that 43% of the traces from the Mg²⁺/RuvC

condition show distinct dynamic features, suggesting that they represent the ~40% RuvC-bound, cleavage-enabled molecules; we, therefore, termed this cluster ‘R’. By contrast, the remaining clusters, termed S1, S2, and S3, dominate in the absence of RuvC and/or presence of Ca²⁺ (Figure 3E, F; Supplementary Figure S10). Consistent with previous reports on the exchange of HJs between the *iso-I*↔*iso-II* conformers in the absence of resolvase (42), these latter clusters exhibit only minor differences in their FRET values and kinetic behaviors and therefore appear to represent HJ_{xh}^R conformational fluctuations, possibly at different branch migration positions, but without RuvC bound.

Notably, a full 84% of all traces in the R-cluster arise from the Mg²⁺/RuvC condition, further supporting a unique behavior associated with Mg²⁺ and RuvC bound HJ_{xh}^R that we identified as cleavage-enabled. The remaining 16% of traces arise from other experimental conditions (5%, 3% and 8% from 5 mM Mg²⁺; from 5 mM Ca²⁺ only; and from 5 mM Ca²⁺ plus 400 nM RuvC, respectively). We expect that noise and photobleaching in the smFRET trajectories will contribute to the cross-contaminating inclusion of the 16% trajectories from non-Mg²⁺/RuvC conditions. Consistent with the notion of unique behavior, the FRET probability distribution of R-cluster traces populates the three conformations *iso-I* (high-FRET), Op (mid-FRET) and *iso-II* (low-FRET), with enrichment of Op from 23% to 50% unique to the Mg²⁺/RuvC condition (compare Figure 3H and B, and Supplementary Figure S10c, d). The existence of FRET efficiency values corresponding to *iso-I* and *iso-II* in these traces suggests that both conformers can be bound by RuvC in a sequence and isoform-independent manner, and with relatively unperturbed interconversion dynamics, consistent with prior observations of the PD complex of RuvC (21). However, the PD complex of HJ₇^{nR} without the cognate cleavage sequence is typically longer-lived (21) (~5 s, Supplementary Figure S11) compared to the very transiently visited (average 0.65 sec, i.e. $t_{1/2} \sim 1.12$ s) PD complex observed here with the cleavable HJ_{xh}^R (Supplementary Figure S12).

A FRET histogram constructed only from the R cluster traces, representing the RuvC bound molecules, is best fitted with three Gaussian peaks that are consistent with the *iso-I*_R ($E_{\text{FRET}} = 0.67 \pm 0.12$), *O*_R ($E_{\text{FRET}} = 0.41 \pm 0.12$) and *iso-II*_R ($E_{\text{FRET}} = 0.15 \pm 0.09$) population (Figure 3G). The transition occupancy density plot (TODP; Figure 3H, Supplementary Figure S10e) generated from over 900 transitions of RuvC-bound R-cluster traces revealed three rapid, reversible conformational transitions: *iso-II*_R↔*iso-I*_R (low↔high-FRET; 21%), *iso-II*_R↔*O*_R (low↔mid-FRET; 57%), and *iso-I*_R↔*O*_R (high↔mid-FRET; 22%), indicating three distinct pairwise transition behaviors across all molecules. Among individual molecules featuring the cleavage-enabled Op state, we observed three different classes of traces (Figure 3I). About 45% traces show only pairwise *iso-II*_R↔*O*_R dynamics, while 10% traces exhibit all three pairwise transitions, indicative of adoption of the PD complex. Interestingly, the remaining 35% traces show a slow interconversion from one to the other dynamic behavior, mainly from *iso-I*_R↔*O*_R↔*iso-II*_R toward *iso-II*_R↔*O*_R (‘mixed-traces’; Figure 3I, Supplementary Figure S13).

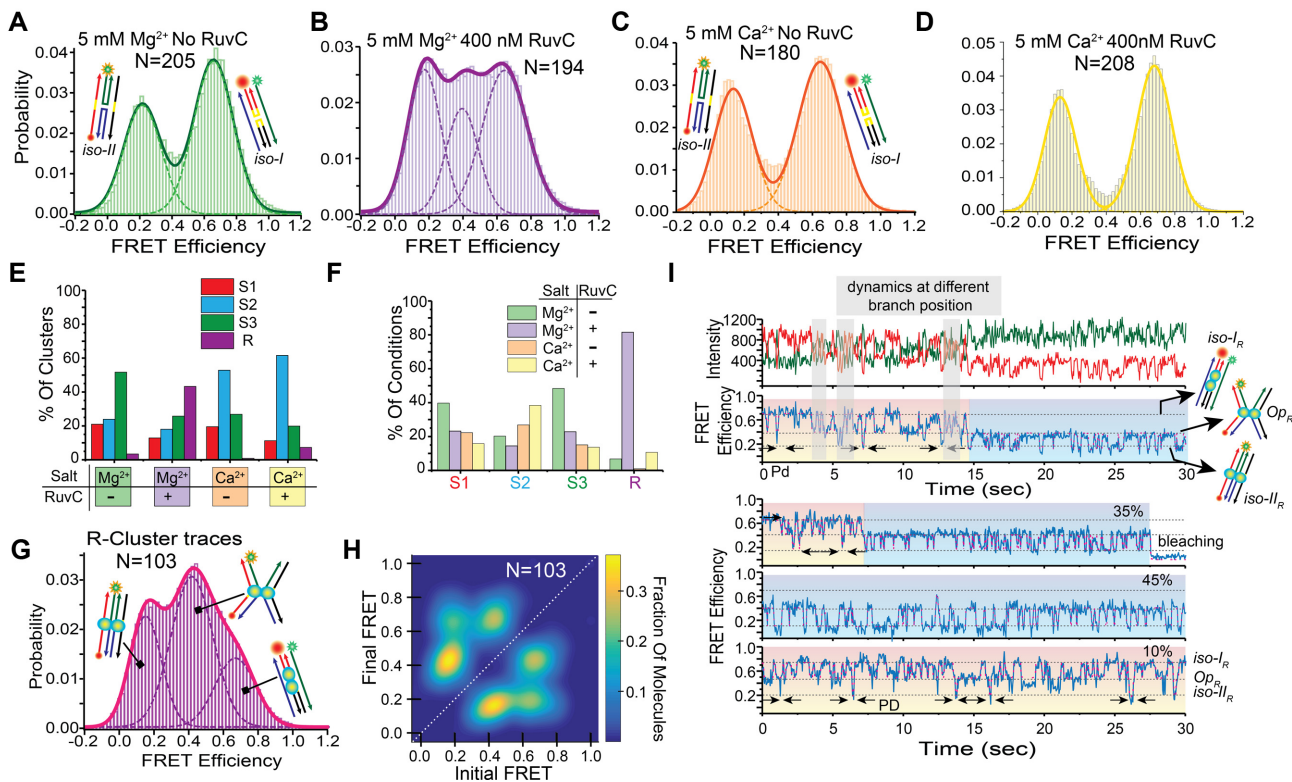


Figure 3. Single molecule cluster analysis (SiMCAn) of smFRET trajectories reveals dynamic behaviors unique to the cleavage-competent RuvC-HJ complex. FRET probability distributions of (A) 5 mM Mg²⁺ without RuvC, (B) 5 mM Mg²⁺ plus 400 nM RuvC (C) 5 mM Ca²⁺ without RuvC, and (D) 5 mM Ca²⁺ plus 400 nM RuvC. Multi-peak Gaussian functions are used to fit each histogram. N indicates the number of molecules used to generate the histogram. Associated structural cartoons depict the conformational states corresponding to each FRET population. (E) Summary of SiMCAn results, showing bar graphs with occupancy of the four clusters found in four experimental conditions. Clusters S1, S2 and S3 are distributed over all different conditions. By contrast, the R-cluster is predominantly found in the 5 mM Mg²⁺ plus 400 nM RuvC condition, indicating that the R-cluster is associated with the RuvC- HJ_{xh}^R complex. (F) Bar graph showing the fraction of molecules from each experimental condition contributing to the four clusters. More than 80% of the molecules in the R-cluster belong to the condition where both Mg²⁺ and RuvC are present. (G) FRET efficiency histogram calculated from the traces belonging to the R-cluster, shown with multi-peak Gaussian fits. Associated cartoons represent different RuvC-HJ complex conformations corresponding to different FRET states. (H) Transition Occupancy Density Plots (TODPs) from R-cluster traces showing the fraction of HJs that undergo conformational transitions from a given initial FRET state to a specific final FRET. Three main sets of bidirectional transitions are observed, representing iso-II_R ↔ O_P_R, iso-I_R ↔ iso-II_R, and iso-I_R ↔ O_P_R behavior, respectively. (I) Representative fluorescence intensity trace of Cy3 (green) and Cy5 (red) fluorophore, FRET efficiency (blue) and HMM fitting (magenta) from the 5 mM Mg²⁺ plus 400 nM RuvC condition (top panel). Three additional FRET efficiency traces show different types of behaviors under the same conditions (bottom panel), with percentages delineating the fractions of traces displaying such behavior. Associated cartoons represent most likely conformations corresponding to each FRET value. The orange background represents iso-II_R ↔ O_P_R behavior and the blue background represents iso-II_R ↔ O_P_R behavior. Sudden visits to non-prevalent FRET states, assigned as RuvC's PD complex (marked by black arrows) and conformer exchange at a different branchpoint position (marked by gray background), are observed in the iso-I_R ↔ O_P_R behavior and absent from the iso-II_R ↔ O_P_R behavior.

To probe the mechanism of the iso-I_R↔O_P_R↔iso-II_R to iso-II_R↔O_P_R interconversion in these mixed traces, we segmented them into early and late phases relative to the time of switching from the iso-I_R↔O_P_R↔iso-II_R dynamics to the pairwise iso-II_R↔O_P_R dynamics. Visual inspection revealed that the conformational dynamics in the two phases are quite different; while the early phase shows complex multistate dynamics, the late phase dynamics are comparably homogeneous with only two states. To further characterize these behaviors, we plotted separate FRET efficiency histograms for the two phases. We found that the early phase indeed shows three different FRET peaks, representing iso-I_R ($E_{\text{FRET}} = 0.64$), O_P_R ($E_{\text{FRET}} = 0.42$), and iso-II_R ($E_{\text{FRET}} = 0.17$; Figure 4A). In contrast, the late phase only displays two FRET peaks, representing O_P_R ($E_{\text{FRET}} = 0.42$) and iso-II_R ($E_{\text{FRET}} = 0.14$; Figure 4B). These observations lead to the hypothesis that access to the

iso-I_R state of the early phase becomes blocked in the late phase.

To further test this hypothesis, we performed a second layer of SiMCAn. Based on differences in their FRET states and transition dynamics the early and the late trace segments become grouped into four distinct clusters, Cl-1 and Cl-2 for the early phases and Cl-3 and Cl-4 for the late phases (Supplementary Figure S14a and S14b). The only differences between Cl-1 and Cl-2 on the one hand and Cl-3 and Cl-4 on the other are slight variations in FRET values, as would be caused by different HJ_{xh}^R branch positions or minor experimental variations. To understand the dynamics of the corresponding phases, we constructed separate TODPs for all Cl-1/Cl-2 trace segments and separately for all Cl-3/Cl-4 segments. The early-phase Cl-1/Cl-2 TODP exhibits iso-I_R↔O_P_R↔iso-II_R transition behavior. That is, the population below the diagonal line in Figure 4C

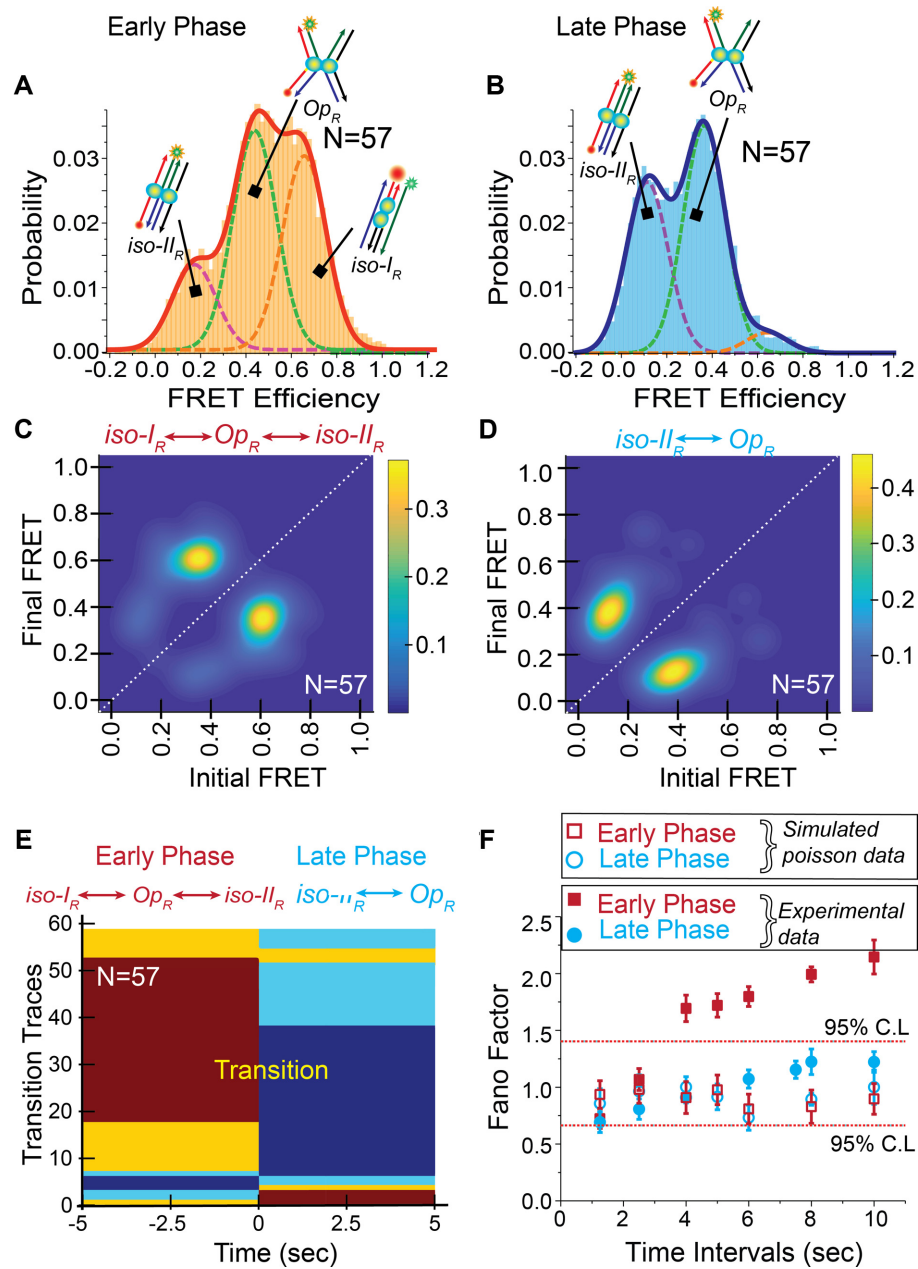


Figure 4. Analysis of the dynamic smFRET traces reveal transitions from the catalytically incompetent RuvC-HJ complex to the cleavage-competent complex. (A) Single molecule FRET efficiency histogram of the early phase of the transition traces. (B) Single molecule FRET efficiency histogram of the late phase of the transition traces. (C) TODP calculated from the early phases of the traces (red/yellow) show only $iso-I_R \leftrightarrow Op_R \leftrightarrow iso-II_R$ behavior. (D) segments from the later phases of the traces (cyan/blue) show $iso-II_R \leftrightarrow Op_R$ behavior. (E) The early and late phases of the mixed R-cluster traces were classified into four clusters (annotated in red, yellow, cyan and blue) using SiMCAn. The early phases, representing $iso-I_R \leftrightarrow Op_R \leftrightarrow iso-II_R$ behavior, and the late phases, representing $iso-II_R \leftrightarrow Op_R$ behavior, belongs to different clusters (Supplementary Figure S14). Upon reconstitution of their early and late phases with their clusters annotated, a clear propensity becomes evident for individual traces to converge over time onto the $iso-II_R \leftrightarrow Op_R$ behavior. (F) The Fano factor was calculated across various time intervals for the $iso-I_R \leftrightarrow Op_R \leftrightarrow iso-II_R$ behavior (solid red square), $iso-II_R \leftrightarrow Op_R$ behavior (solid blue circle) and simulated Poisson data same in length and number of traces for the same behaviors (open red square, open blue circle) respectively. The dashed lines indicate the 95% confidence level of the data. The early phase $iso-I_R \leftrightarrow Op_R \leftrightarrow iso-II_R$ behavior Fano factor values deviate from 1, indicating a non-random underlying distribution, while the late phase iso-II-loaded $iso-II_R \leftrightarrow Op_R$ behavior Fano factor data remain close to 1, indicating a Poisson distribution.

transitions from an initial $E_{\text{FRET}} = \sim 0.65$ to a final $E_{\text{FRET}} = \sim 0.4$, whereas the population above the diagonal does the opposite. This pair of populations – symmetric relative to the diagonal—represent reversible conformational transitions between the two FRET states of iso-I ($E_{\text{FRET}} = \sim 0.65$) and Op ($E_{\text{FRET}} = \sim 0.4$), with occasional excursions into iso-II_R ($E_{\text{FRET}} = 0.14$). By contrast, as expected from Figure 4B the late-phase Cl-3/Cl-4 TODP displays almost exclusively $O_{\text{pR}} \leftrightarrow \text{iso-II}_R$ transition behavior between low-FRET ($\text{iso-II}_R E_{\text{FRET}} = \sim 0.15$) and mid-FRET ($O_{\text{pR}} E_{\text{FRET}} = \sim 0.4$), respectively (Figure 4D). A rastergram summarizing the early and late phases for all molecules shows a strong propensity (>90% probability) to start from $\text{iso-I}_R \leftrightarrow O_{\text{pR}} \leftrightarrow \text{iso-II}_R$ behavior (as grouped in Cl-1/Cl-2) and to end with $\text{iso-II}_R \leftrightarrow O_{\text{pR}}$ behavior (as grouped in Cl-3/Cl-4; Figure 4E). Consistent with this time dependent progression, we observed an increase from 20% to 32% in the number of traces exhibiting such $\text{iso-I}_R \leftrightarrow O_{\text{pR}} \leftrightarrow \text{iso-II}_R$ to $\text{iso-II}_R \leftrightarrow O_{\text{pR}}$ interconversion when observing successive fields of view over a 60 min time window (Supplementary Figure S14b). Such a progressive, seemingly irreversible change from $\text{iso-I}_R \leftrightarrow O_{\text{pR}} \leftrightarrow \text{iso-II}_R$ to $\text{iso-II}_R \leftrightarrow O_{\text{pR}}$ behavior signifies a structural rearrangement of the HJ-RuvC complex, accompanied by stabilization of the catalytically competent (iso-II_R) conformation at the occlusion of the cleavage-incompetent iso-I_R , as will be required for RuvC mediated cleavage of HJ_{xh}^R.

A detailed Fano-factor analysis further supports this conformational switch model. Generally, a Fano factor determines the variability in number of pairwise transitions relative to its mean; values >1 indicate non-Poisson behavior while a value of 1 represents a random Poisson process (33,34). Significantly, we found that the Fano factor of the early phase is >1, whereas the Fano factor of the late phase remains around the Poissonian 1 (more precisely, within 95% confidence level of a Fano factor of 1) over arbitrarily chosen observation windows (Figure 4F). A non-Poisson Fano factor of >1 was also found for the dynamics of HJ_{xh}^R in the absence of RuvC, where different branch points can be freely visited over time (Supplementary Figure S15), forming a nonrandom behavior. Although the variation in the Fano-factor calculated from the late-phase dynamics is slightly greater than expected from simulated Poisson behavior, this variation is well within experimental error, as indicated by the two horizontal lines representing the 95% confidence level of the data, and consistent with previously published work (43). By contrast, the early-phase data are clearly distinct from the late phase data since their Fano-factor varies >95% confidence line would allow. Thus, only the early phase shows co-existence of conformer isomerization and branch migration. Complementarily, cross-correlation analysis of the donor and acceptor intensities indicates slower kinetics in the late phase than in the early phase (Supplementary Figure S16).

Taken together, our observations corroborate the notion that, once RuvC has reached the consensus sequence of HJ_{xh}^R through branch migration, the complex converts to the late phase by blocking further branch migration, suppressing access to the cleavage-incompetent iso-I_R state, and adopting more stable contacts with the consensus sequence in the enzyme active site. That is, whereas the early phase

still allows for PD-complex mediated conformer exchange while exploring different branch points, the late phase locks the HJ-RuvC complex into more limited conformational dynamics with stronger protein-DNA interactions as a prelude to cleavage.

DISCUSSION

Homologous recombination plays a critical role in maintaining a cell's balance between genetic stability and diversity, requiring a highly controlled pathway of low error rate (44). As such, the site-specific cleavage of two of the four DNA strands of a HJ by the bacterial resolvase RuvC needs to be a relatively rare, but precise event. The recent work by Zhou *et al.* focused on the protein binding kinetics and multivalent binding capacity of RuvC, which enables it to partially dissociate from a non-cleavable HJ to allow the intrinsic HJ conformational dynamics to continue. Specific constraints, in particular the use of Ca²⁺ instead of Mg²⁺ (the latter a strict requirement for RuvC mediated cleavage) and the absence of a cognate cleavage sequence, were put in place to focus on the multivalent binding nature of RuvC and resulting HJ dynamics only. How the HJ-RuvC complex advances to cleavage upon recognition of a cleavable sequence therefore remained unanswered. Our understanding of the highly sequence selective cleavage of HJs by *E. coli* RuvC is held back by the lack of a crystal structure of the complex (i.e. *E. coli* RuvC-HJ_{xh}^R), leaving many questions open. Here we use smFRET analysis of a variety of substrates and conditions together with cluster analysis to derive a model for how such precision is achieved (Figure 5). Applying two layers of the established model-independent cluster analysis method SiMCAn (35,36) helped to decouple the dynamics of HJ-only molecules from those of HJ-RuvC complexes without the risk of expectation bias, especially when the trajectories are complex. We observe that the binding of RuvC is HJ isoform independent (and thus independent of the positioning of the cognate sequence) while still supporting the intrinsic isomerization dynamics of both cleavable and non-cleavable HJs via partial dissociation of the protein (PD complex), consistent with the recent report by Zhou *et al.* (21). Beyond, we discover that RuvC in fact takes advantage of the intrinsic dynamics of the cleavable HJ to scan for and then kinetically trap the catalytically active conformation through a 'snap-lock' conformational switch. After this switch, the loosely associated PD complex is no longer visited so that slower conformer isomerization kinetics ensue, consistent with stabilization of the RuvC-HJ complex upon accommodation of the cleavable cognate sequences in the dimeric resolvase active sites (Figure 5).

Global and local conformational dynamics leading to allosteric communication within a structure represent a general mechanism adopted by enzymes to control their substrate specificity. Indeed, our model of rapid substrate scanning via a loosely associated complex, followed by stabilization of a snap-locked conformation once a recognized sequence is accommodated in the enzyme active site (Figure 5) is strikingly consistent with the mode of action of other DNA-modifying proteins, including DNA repair enzymes (45) and endonucleases such as CRISPR-Cas9 (46). For example, an increased population of the cleavage-competent

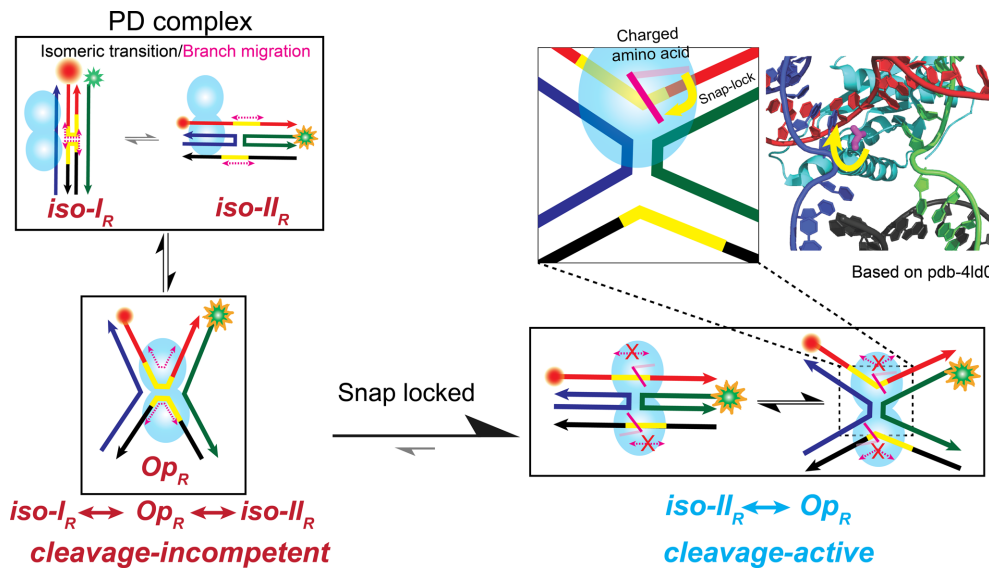


Figure 5. Proposed model for RuvC-mediated scanning and site-specific cleavage. When RuvC binds to the HJ, it fluctuates between a loosely bound PD complex that allows the HJ junction to maintain its dynamic $iso\text{-}I_R \leftrightarrow iso\text{-}II_R$ exchange and the more tightly bound, shallow-angle Op_R state. Branch migration can occur at this stage, allowing RuvC to scan for the cleavable cognate sequence. Once a cognate sequence is found, the Op_R state undergoes a interconversion, wherein each cleavage site is snap-locked by a stacking amino acid, disallowing branch migration and adoption of the PD complex and $iso\text{-}I_R$ conformation.

state is observed when the interaction of Cas9 and DNA is stabilized in the presence of perfect match (47). Such a search mechanism affords high fidelity at low energetic cost and has been referred to as conformational proofreading (48–50); the resulting kinetic trap is resolved upon Mg^{2+} -assisted substrate cleavage and dissociation of the resolvase from the disentangled products.

Inspection of the available crystal structures of RuvC-HJ complexes provides further mechanistic underpinnings for our model. The DNA binding cleft in the RuvC monomer, the surface of which is covered by basic residues, is found to be $\sim 20\text{--}25\text{ \AA}$ wide and 20 \AA deep and thus sufficiently large to accommodate a DNA duplex (13). In the active dimer, the catalytic centers are reported to be $\sim 30\text{ \AA}$ apart (13). More than twelve amino acids from each monomer of RuvC form redundant contacts with the HJ (11), allowing the resolvase to break some interactions in the loosely associated PD complex while the HJ undergoes unimpeded transitions between $iso\text{-}I$ and $iso\text{-}II$ as well as branch migration (Figure 5) (21). The catalytic center of *E. coli* RuvC is constituted of four acidic residues Asp7, Asp66, Asp138 and Asp141 (7), located at the bottom of the cleft whose surface is covered by multiple basic residues (13). Previous studies have shown that these acidic and basic residues play critical roles in forming the catalytically active complex (51). Additionally, it has been posited that the aromatic ring of Phe69 in *E. coli* RuvC forms a stacking interaction with a nucleotide base (52), thereby offering a plausible basis for the snap-locking conformational switch en route to site-specific catalysis our studies reveal, since such stacking would plausibly halt branch migration (Figure 5). Accordingly, the mutation of Phe69 has been reported to lead to the loss of repair activity by RuvC (13). A recent report used molecular dynamics simulations based on crystal structures of a thermostable *Thermus thermophilus* (Tt) RuvC to pro-

pose that cognate sequence recognition leads to an induced fit wherein Arg76 disrupts the scissile A-T base pair, exposing the thymine residue to the active site for catalysis (25). Consistent with our model in Figure 5, the authors observed protein-assisted base flipping in a resolvable HJ with consensus sequence but not in an unresolvable HJ (25). A similar mechanism of protein-assisted scissile base flipping was also reported for plant resolvases (53). A sequence alignment of *E. coli* and Tt RuvC reveals that residue Lys72, which is one of eight basic residues in the cleft, may play a similar role in *E. coli* RuvC as Arg76 in Tt (11).

Conversely, a lack of an available cleavable cognate sequence for one RuvC monomer is known to disrupt the favorable positioning of the consensus sequence in the active site of the other RuvC monomer, suggesting that non-cleavable junction sequences may generally form fewer specific contacts (54). In further support of this notion, we find that the highly dynamic PD complex of the non-cleavable $HJ_{7^{NR}}$ persists while that of the cleavable HJ_{xh}^R is lost upon site-specific recognition and snap-locking into the slower late-phase $iso\text{-}II_R \leftrightarrow Op_R$ only transitions.

In conclusion, our findings provide a mechanistic picture underscoring the importance of conformational and branch migration dynamics in HJ resolution. RuvC achieves accurate HJ resolution as a key step in homologous recombination by conformational proofreading, where it first exploits dynamics intrinsic to an HJ to find a cognate sequence, and then constrains (snap-locks) the dynamics to achieve site-specific cleavage. Our findings thus may inspire further studies using site-specific mutation of the active site of RuvC and computational investigation to determine specific residues responsible for the snap-locking mechanism. This mechanism of RuvC may also open exciting avenues toward antimicrobial therapies (55,56) since sequence selectivity distinguishes RuvC from many eukaryotic and mam-

malian HJ resolvases (57–61). Additionally, we anticipate that our quantitative cluster analysis will serve as a powerful tool to unravel the differentiating mechanisms of other DNA binding and processing enzymes that employ conformational proofreading to achieve functional fidelity.

DATA AVAILABILITY

The data that support the findings of this study are available from the corresponding author upon reasonable request.

SUPPLEMENTARY DATA

Supplementary Data are available at NAR Online.

ACKNOWLEDGEMENTS

We thank Dr Alexander Johnson-Buck for careful reading of the manuscript and thoughtful suggestions.

FUNDING

NSF Award [DMR-1607854]; NIH [GM062357 and GM131922 to N.G.W]. Funding for open access charge: NIH.

Conflict of interest statement. None declared.

REFERENCES

- Li,X. and Heyer,W.-D. (2008) Homologous recombination in DNA repair and DNA damage tolerance. *Cell Res.*, **18**, 99–113.
- Jasin,M. and Rothstein,R. (2013) Repair of strand breaks by homologous recombination. *Cold Spring Harb. Perspect. Biol.*, **5**, a012740.
- Sarbajna,S. and West,S.C. (2014) Holliday junction processing enzymes as guardians of genome stability. *Trends Biochem. Sci.*, **39**, 409–419.
- Wright,W.D., Shah,S.S. and Heyer,W.D. (2018) Homologous recombination and the repair of DNA double-strand breaks. *J. Biol. Chem.*, **293**, 10524–10535.
- Scully,R., Panday,A., Elango,R. and Willis,N.A. (2019) DNA double-strand break repair-pathway choice in somatic mammalian cells. *Nat. Rev. Mol. Cell Biol.*, **20**, 698–714.
- Shah,R., Bennett,R.J. and West,S.C. (1994) Genetic recombination in *E. coli*: RuvC protein cleaves Holliday junctions at resolution hotspots in vitro. *Cell*, **79**, 853–864.
- Bennett,R.J. and West,S.C. (1995) RuvC protein resolves Holliday junctions via cleavage of the continuous (noncrossover) strands. *Proc. Natl Acad. Sci. U.S.A.*, **92**, 5635–5639.
- Shida,T., Iwasaki,H., Saito,A., Kyogoku,Y. and Shinagawa,H. (1996) Analysis of substrate specificity of the RuvC holliday junction resolvase with synthetic Holliday junctions. *J. Biol. Chem.*, **271**, 26105–26109.
- Yamada,K., Ariyoshi,M. and Morikawa,K. (2004) Three-dimensional structural views of branch migration and resolution in DNA homologous recombination. *Curr. Opin. Struct. Biol.*, **14**, 130–137.
- Michel,B., Sinha,A.K. and Leach,D.R.F. (2018) Replication fork breakage and restart in *Escherichia coli*. *Microbiol. Mol. Biol. Rev.*, **82**, e00013-18.
- Gorecka,K.M., Komorowska,W. and Nowotny,M. (2013) Crystal structure of RuvC resolvase in complex with Holliday junction substrate. *Nucleic Acids Res.*, **41**, 9945–9955.
- Chen,L., Shi,K., Yin,Z. and Aihara,H. (2013) Structural asymmetry in the *Thermus thermophilus* RuvC dimer suggests a basis for sequential strand cleavages during Holliday junction resolution. *Nucleic Acids Res.*, **41**, 648–656.
- Ariyoshi,M., Vassylyev,D.G., Iwasaki,H., Nakamura,H., Shinagawa,H. and Morikawa,K. (1994) Atomic structure of the RuvC resolvase: a holliday junction-specific endonuclease from *E. coli*. *Cell*, **78**, 1063–1072.
- Bennett,R.J., Dunderdale,H.J. and West,S.C. (1993) Resolution of Holliday junctions by RuvC resolvase: cleavage specificity and DNA distortion. *Cell*, **74**, 1021–1031.
- Bennett,R.J. and West,S.C. (1995) Structural analysis of the RuvC-Holliday junction complex reveals an unfolded junction. *J. Mol. Biol.*, **252**, 213–226.
- Wyatt,H.D. and West,S.C. (2014) Holliday junction resolvases. *Cold Spring Harb. Perspect. Biol.*, **6**, a023192.
- Nowakowski,J., Shim,P.J., Prasad,G.S., Stout,C.D. and Joyce,G.F. (1999) Crystal structure of an 82-nucleotide RNA-DNA complex formed by the 10-23 DNA enzyme. *Nat. Struct. Biol.*, **6**, 151–156.
- Eichman,B.F., Vargason,J.M., Mooers,B.H. and Ho,P.S. (2000) The Holliday junction in an inverted repeat DNA sequence: sequence effects on the structure of four-way junctions. *Proc. Natl Acad. Sci. U.S.A.*, **97**, 3971–3976.
- McKinney,S.A., Declais,A.C., Lilley,D.M. and Ha,T. (2003) Structural dynamics of individual Holliday junctions. *Nat. Struct. Biol.*, **10**, 93–97.
- Joo,C., McKinney,S.A., Lilley,D.M. and Ha,T. (2004) Exploring rare conformational species and ionic effects in DNA Holliday junctions using single-molecule spectroscopy. *J. Mol. Biol.*, **341**, 739–751.
- Zhou,R., Yang,O., Déclais,A.-C., Jin,H., Gwon,G.H., Freeman,A.D.J., Cho,Y., Lilley,D.M.J. and Ha,T. (2019) Junction resolving enzymes use multivalency to keep the Holliday junction dynamic. *Nat. Chem. Biol.*, **15**, 269–275.
- Bennett,R.J. and West,S.C. (1996) Resolution of Holliday junctions in genetic recombination: RuvC protein nicks DNA at the point of strand exchange. *Proc. Natl Acad. Sci. U.S.A.*, **93**, 12217–12222.
- White,M.F., Giraud-Panis,M.J., Pohler,J.R. and Lilley,D.M. (1997) Recognition and manipulation of branched DNA structure by junction-resolving enzymes. *J. Mol. Biol.*, **269**, 647–664.
- Fogg,J.M., Schofield,M.J., White,M.F. and Lilley,D.M. (1999) Sequence and functional-group specificity for cleavage of DNA junctions by RuvC of *Escherichia coli*. *Biochemistry*, **38**, 11349–11358.
- Gorecka,K.M., Krepl,M., Szlachcic,A., Poznanski,J., Sponer,J. and Nowotny,M. (2019) RuvC uses dynamic probing of the Holliday junction to achieve sequence specificity and efficient resolution. *Nat. Commun.*, **10**, 4102.
- Joo,C., Balci,H., Ishitsuka,Y., Buranachai,C. and Ha,T. (2008) Advances in single-molecule fluorescence methods for molecular biology. *Annu. Rev. Biochem.*, **77**, 51–76.
- Suddala,K.C. and Walter,N.G. (2014) Riboswitch structure and dynamics by smFRET microscopy. *Methods Enzymol.*, **549**, 343–373.
- Juette,M.F., Terry,D.S., Wasserman,M.R., Altman,R.B., Zhou,Z., Zhao,H. and Blanchard,S.C. (2016) Single-molecule imaging of non-equilibrium molecular ensembles on the millisecond timescale. *Nat. Methods*, **13**, 341–344.
- Blanco,M. and Walter,N.G. (2010) Analysis of complex single-molecule FRET time trajectories. *Methods Enzymol.*, **472**, 153–178.
- Boehm,E.M., Subramanyam,S., Ghoneim,M., Washington,M.T. and Spies,M. (2016) Quantifying the assembly of multicomponent molecular machines by single-molecule total internal reflection fluorescence microscopy. *Methods Enzymol.*, **581**, 105–145.
- Sung,J., Sivaramakrishnan,S., Dunn,A.R. and Spudich,J.A. (2010) Single-molecule dual-beam optical trap analysis of protein structure and function. *Methods Enzymol.*, **475**, 321–375.
- Okamoto,K. and Terazima,M. (2008) Distribution analysis for single molecule FRET measurement. *J. Phys. Chem. B*, **112**, 7308–7314.
- Eden,U.T. and Kramer,M.A. (2010) Drawing inferences from Fano factor calculations. *J. Neurosci. Methods*, **190**, 149–152.
- Rinaldi,A.J., Lund,P.E., Blanco,M.R. and Walter,N.G. (2016) The Shine-Dalgarno sequence of riboswitch-regulated single mRNAs shows ligand-dependent accessibility bursts. *Nat. Commun.*, **7**, 8976.
- Rohlman,C.E., Blanco,M.R. and Walter,N.G. (2016) Putting humpty-dumpty together: clustering the functional dynamics of single biomolecular machines such as the spliceosome. *Methods Enzymol.*, **581**, 257–283.

36. Blanco,M.R., Martin,J.S., Kahlscheuer,M.L., Krishnan,R., Abelson,J., Laederach,A. and Walter,N.G. (2015) Single molecule cluster analysis dissects splicing pathway conformational dynamics. *Nat. Methods*, **12**, 1077–1084.
37. McKinney,S.A., Freeman,A.D., Lilley,D.M. and Ha,T. (2005) Observing spontaneous branch migration of Holliday junctions one step at a time. *Proc. Natl Acad. Sci. U.S.A.*, **102**, 5715–5720.
38. Hohng,S., Zhou,R., Nahas,M.K., Yu,J., Schulten,K., Lilley,D.M. and Ha,T. (2007) Fluorescence-force spectroscopy maps two-dimensional reaction landscape of the holliday junction. *Science*, **318**, 279–283.
39. Tang,J., Sun,Y., Pang,S. and Han,K.Y. (2017) Spatially encoded fast single-molecule fluorescence spectroscopy with full field-of-view. *Sci. Rep.*, **7**, 10945.
40. Miick,S.M., Fee,R.S., Millar,D.P. and Chazin,W.J. (1997) Crossover isomer bias is the primary sequence-dependent property of immobilized Holliday junctions. *Proc. Natl Acad. Sci. U.S.A.*, **94**, 9080–9084.
41. Takahagi,M., Iwasaki,H. and Shinagawa,H. (1994) Structural requirements of substrate DNA for binding to and cleavage by RuvC, a Holliday junction resolvase. *J. Biol. Chem.*, **269**, 15132–15139.
42. Hyeon,C., Lee,J., Yoon,J., Hohng,S. and Thirumalai,D. (2012) Hidden complexity in the isomerization dynamics of Holliday junctions. *Nat. Chem.*, **4**, 907–914.
43. Rinaldi,A.J., Lund,P.E., Blanco,M.R. and Walter,N.G. (2016) The Shine-Dalgarno sequence of riboswitch-regulated single mRNAs shows ligand-dependent accessibility bursts. *Nat. Commun.*, **7**, 8976.
44. Guirouilh-Barbat,J., Lambert,S., Bertrand,P. and Lopez,B.S. (2014) Is homologous recombination really an error-free process? *Front Genet*, **5**, 175.
45. Yang,W. (2008) Structure and mechanism for DNA lesion recognition. *Cell Res.*, **18**, 184–197.
46. Sternberg,S.H., LaFrance,B., Kaplan,M. and Doudna,J.A. (2015) Conformational control of DNA target cleavage by CRISPR-Cas9. *Nature*, **527**, 110–113.
47. Yang,M., Peng,S., Sun,R., Lin,J., Wang,N. and Chen,C. (2018) The conformational dynamics of Cas9 governing DNA cleavage are revealed by single-molecule FRET. *Cell Rep.*, **22**, 372–382.
48. Savir,Y. and Tlusty,T. (2007) Conformational proofreading: the impact of conformational changes on the specificity of molecular recognition. *PLoS One*, **2**, e468.
49. Globty,V., Kim,S.H. and Joo,C. (2018) Single-molecule view of small RNA-guided target search and recognition. *Annu. Rev. Biophys.*, **47**, 569–593.
50. Walter,N.G. (2019) Biological pathway specificity in the cell—does molecular diversity matter? *Bioessays*, **41**, e1800244.
51. Yoshikawa,M., Iwasaki,H., Kinoshita,K. and Shinagawa,H. (2000) Two basic residues, Lys-107 and Lys-118, of RuvC resolvase are involved in critical contacts with the Holliday junction for its resolution. *Genes Cells*, **5**, 803–813.
52. Yoshikawa,M., Iwasaki,H. and Shinagawa,H. (2001) Evidence that phenylalanine 69 in Escherichia coli RuvC resolvase forms a stacking interaction during binding and destabilization of a Holliday junction DNA substrate. *J. Biol. Chem.*, **276**, 10432–10436.
53. Lin,H., Zhang,D., Zuo,K., Yuan,C., Li,J., Huang,M. and Lin,Z. (2019) Structural basis of sequence-specific Holliday junction cleavage by MOC1. *Nat. Chem. Biol.*, **15**, 1241–1248.
54. Shah,R., Cosstick,R. and West,S.C. (1997) The RuvC protein dimer resolves Holliday junctions by a dual incision mechanism that involves base-specific contacts. *EMBO J.*, **16**, 1464–1472.
55. Loughlin,M.F., Barnard,F.M., Jenkins,D., Sharples,G.J. and Jenks,P.J. (2003) Helicobacter pylori mutants defective in RuvC Holliday junction resolvase display reduced macrophage survival and spontaneous clearance from the murine gastric mucosa. *Infect. Immun.*, **71**, 2022–2031.
56. Garcia,A.D., Otero,J., Lebowitz,J., Schuck,P. and Moss,B. (2006) Quaternary structure and cleavage specificity of a poxvirus holliday junction resolvase. *J. Biol. Chem.*, **281**, 11618–11626.
57. Wyatt,H.D., Sarbajna,S., Matos,J. and West,S.C. (2013) Coordinated actions of SLX1-SLX4 and MUS81-EME1 for Holliday junction resolution in human cells. *Mol. Cell*, **52**, 234–247.
58. Ciccia,A., Constantinou,A. and West,S.C. (2003) Identification and characterization of the human mus81-eme1 endonuclease. *J. Biol. Chem.*, **278**, 25172–25178.
59. Chen,X.B., Melchionna,R., Denis,C.M., Gaillard,P.H., Blasina,A., Van de Weyer,I., Boddy,M.N., Russell,P., Vialard,J. and McGowan,C.H. (2001) Human Mus81-associated endonuclease cleaves Holliday junctions in vitro. *Mol. Cell*, **8**, 1117–1127.
60. Ip,S.C., Rass,U., Blanco,M.G., Flynn,H.R., Skehel,J.M. and West,S.C. (2008) Identification of Holliday junction resolvases from humans and yeast. *Nature*, **456**, 357–361.
61. Sobhy,M.A., Bralic,A., Raducanu,V.S., Takahashi,M., Tehseen,M., Rashid,F., Zaher,M.S. and Hamdan,S.M. (2019) Resolution of the Holliday junction recombination intermediate by human GEN1 at the single-molecule level. *Nucleic Acids Res.*, **47**, 1935–1949.

Supplementary Materials

Single bacterial resolvases first exploit, then constrain intrinsic dynamics of the Holliday junction to direct recombination

Sujay Ray^{1,†}, Nibedita Pal^{1,†} and Nils G. Walter^{1,*}

¹ Single Molecule Analysis Group, Department of Chemistry, University of Michigan Ann Arbor, Michigan 48109, USA

† These authors contributed equally: Sujay Ray; Nibedita Pal.

* To whom correspondence should be addressed. Email: nwalter@umich.edu

Present Address: [Sujay Ray], Wyss Institute for Biologically Inspired Engineering at Harvard University, Boston, Massachusetts 02115, USA. [Nibedita Pal], Indian Institute of Science Education and Research (IISER) Tirupati, Tirupati 517507, Andhra Pradesh, India.

Supplementary Table S1: List of the DNA oligonucleotides used to assemble our HJs.

| Construct Name | Sequence |
|----------------------------------|---------------------------------------|
| HJ _{xh} ^R -b | 5'-Cy3-GGCCGAAGCAATCGCGCCG-3' |
| HJ _{xh} ^R -h | 5'-CGGCGCGATTGGAGGGGTGG-3' |
| HJ _{xh} ^R -r | 5'-Biotin-CCACCCCTCCAATCACCCGG-3' |
| HJ _{xh} ^R -x | 5'-Cy5-CCGGGTGATTGCTTCCC GCC-3' |
| HJ ₇ ^{nR} -b | 5'- CCTCCCTAGCAAGCCGCTGCTACGG -3' |
| HJ ₇ ^{nR} -h | 5'- Cy3-CCGTAGCAGCGCGAGCGGTGGG -3' |
| HJ ₇ ^{nR} -r | 5'- Biotin-CCCACCGCTCGGCTCAACTGGG -3' |
| HJ ₇ ^{nR} -x | 5'- CCCAGTTGAGCGCTTGCTAGGG-Cy5 -3' |
| HJ ₃ ^{nR} -b | 5'-Cy5-CCTAGCAAGGGCTGCTACG-3' |
| HJ ₃ ^{nR} -h | 5'- CGTAGCAGCCTGAGCGGTGG -3' |
| HJ ₃ ^{nR} -r | 5'-Biotin-CCACCGCTCAACTCAACTGG -3' |
| HJ ₃ ^{nR} -x | 5'- Cy3-CCAGTTGAGTCCTTGCTAGG -3' |

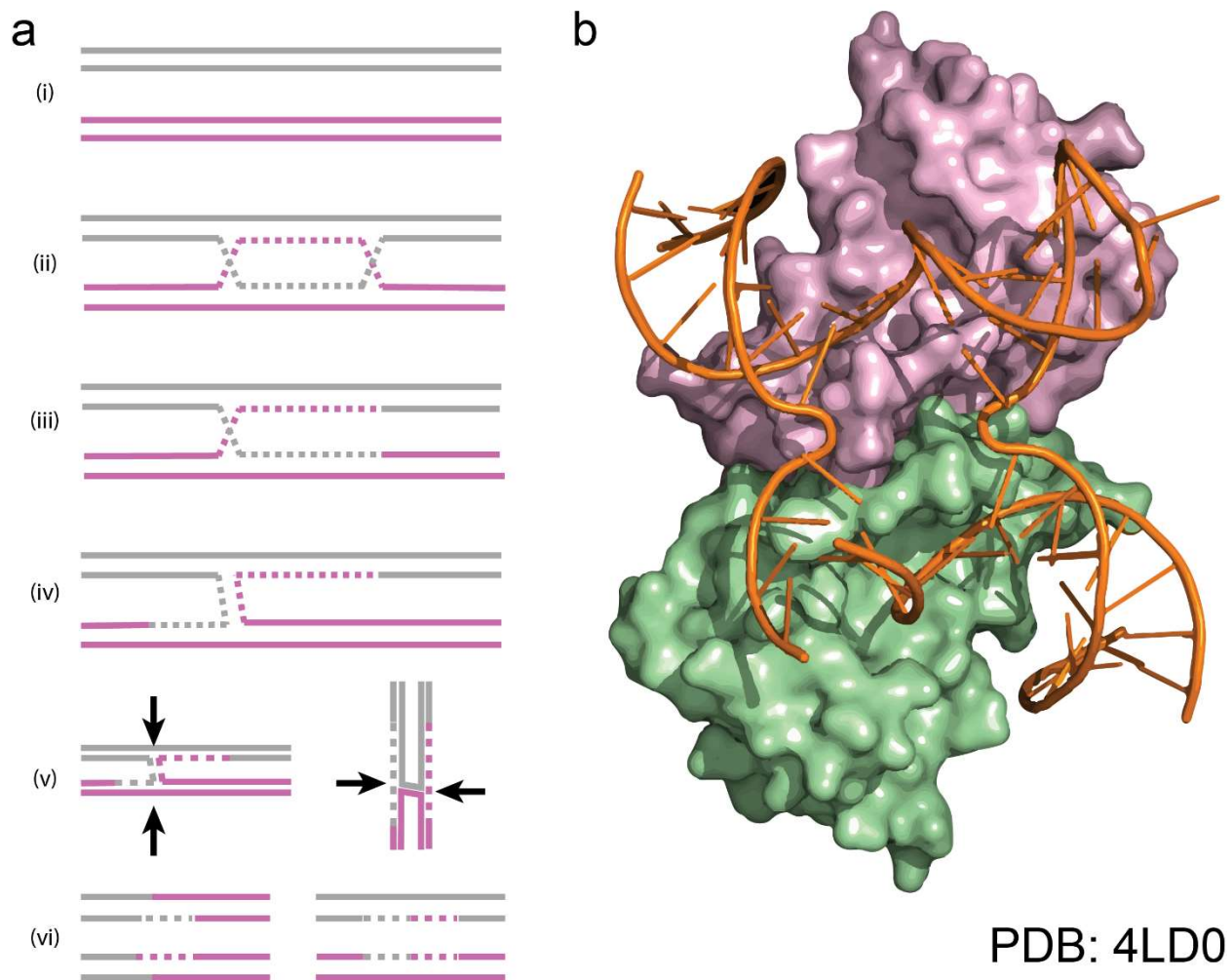
Supplementary Table S2: List of FRET efficiency values, corresponding population percentage, and transition rates for all experiments.

| HJ | Experimental conditions | E _{FRET} value (fraction) of <i>iso-I</i> | E _{FRET} value (fraction) of Op | E _{FRET} value (fraction) of <i>iso-II</i> | k _{I→II} (s ⁻¹) | k _{II→I} (s ⁻¹) |
|-------------------------------|---|---|---|--|--|--|
| HJ _{xh} ^R | 5 mM Mg ²⁺ | 0.65±0.12 (60%) | -- | 0.21±0.11 (40%) | 2.8±0.3 | 4.0±0.4 |
| HJ _{xh} ^R | 10 mM Mg ²⁺ | 0.67±0.11 (59%) | -- | 0.15±0.08 (41%) | 1.7±0.1 | 2.3±0.3 |
| HJ _{xh} ^R | 25 mM Mg ²⁺ | 0.71±0.11 (57%) | -- | 0.15±0.09 (42%) | 1.2±0.2 | 1.4±0.4 |
| HJ _{xh} ^R | 5 mM Mg ²⁺ , 400 nM RuvC | 0.64±0.13 (44%) | 0.40±0.1 (24%) | 0.17±0.10 (32%) | | |
| HJ _{xh} ^R | 5 mM Mg ²⁺ , 400 nM RuvC (R-cluster traces) | 0.67±0.11 (22%) | 0.41±0.1 (50%) | 0.15±0.10 (28%) | k _{O_p→II} (s ¹) k _{II→O_p} (s ¹) k _{O_p→I} (s ⁻¹) k _{I→O_p} (s ⁻¹) k _{I→II} (s ⁻¹) k _{II→I} (s ⁻¹) | 2.5 3.7 3.7 2.8 3.4 4.0 |
| HJ _{xh} ^R | 5 mM Ca ²⁺ | 0.65±0.11 (59%) | -- | 0.14±0.10 (41%) | 3.1±0.4 | 4.3±0.7 |
| HJ _{xh} ^R | 5 mM Ca ²⁺ , 400 nM RuvC | 0.68±0.09 (59%) | -- | 0.15±0.08 (41%) | 2.9±0.3 | 2.3±0.2 |
| HJ _{3n} ^R | 5 mM Mg ²⁺ | 0.50±0.12 (20%) | -- | 0.22±0.13 (80%) | -- | -- |
| HJ _{3n} ^R | 10 mM Mg ²⁺ | 0.55±0.19 (33%) | -- | 0.17±0.10 (67%) | 14.3± | 5.9± |
| HJ _{3n} ^R | 25 mM Mg ²⁺ | 0.62±0.20 (35%) | -- | 0.17±0.12 (65%) | 12.5± | 5.6± |

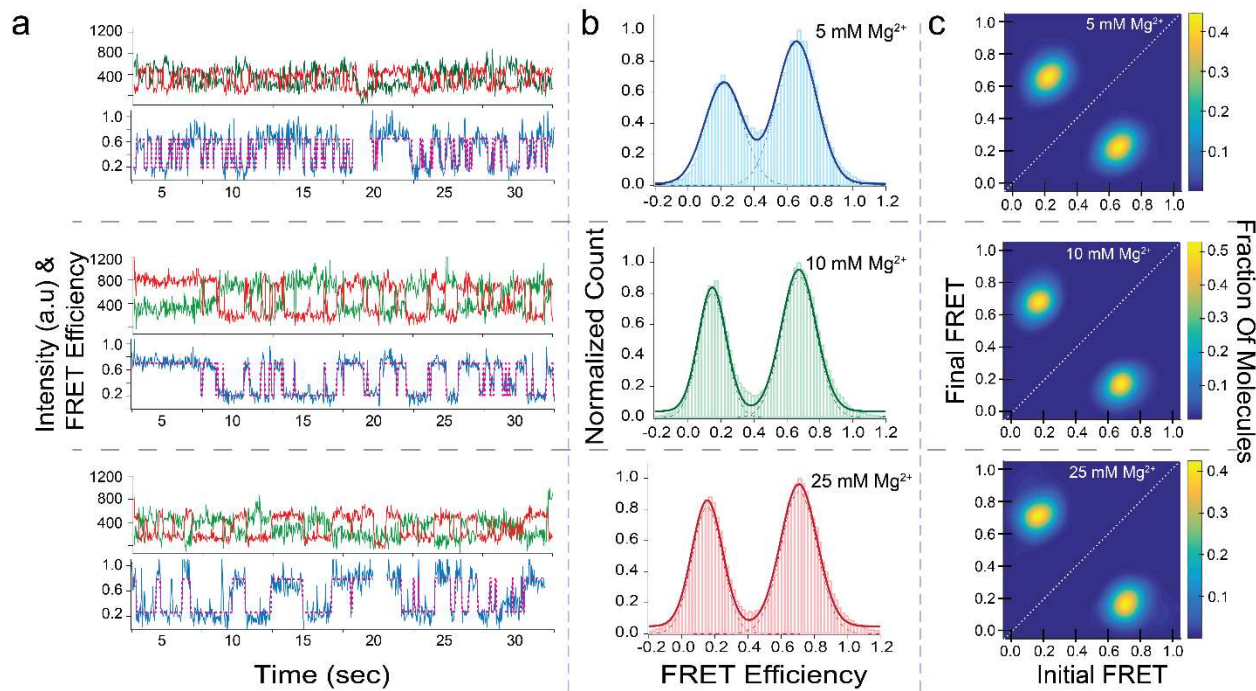
Supplementary Table S3: Summary of complex formation simulation using the software package NUPACK (<http://www.nupack.org/>).

| Strands used | Concentration | Conditions | Complexes formed (expected concentration) |
|--------------|--|--------------------------------|--|
| B, X, H, R | 2 μ M, 2 μ M, 1 μ M, 1 μ M | 500 mM Na ⁺ , 25°C. | Complete HJ (0.89 μ M), B-X (1 μ M), H-R (0.02 μ M), B (0.005 μ M), X (0.005 μ M), H (1×10^{-6} μ M), R (0.5×10^{-6} μ M), R-X-B (0.1×10^{-6} μ M) |
| B, X, H, R | 2 μ M, 2 μ M, 2 μ M, 2 μ M | 500 mM Na ⁺ , 25°C. | Complete HJ (1.8 μ M), B-X (0.2 μ M), H-R (0.2 μ M), B (0.002 μ M), X (0.002 μ M), H (3×10^{-6} μ M), R (2×10^{-6} μ M), R-X-B (3×10^{-9} μ M) |
| B, X, R | 2 μ M, 2 μ M, 2 μ M | 500 mM Na ⁺ , 25°C. | B-X (1.8 μ M), R (1.8 μ M), B (0.2 μ M), R-X (0.2 μ M), R-X-B (0.03 μ M) |

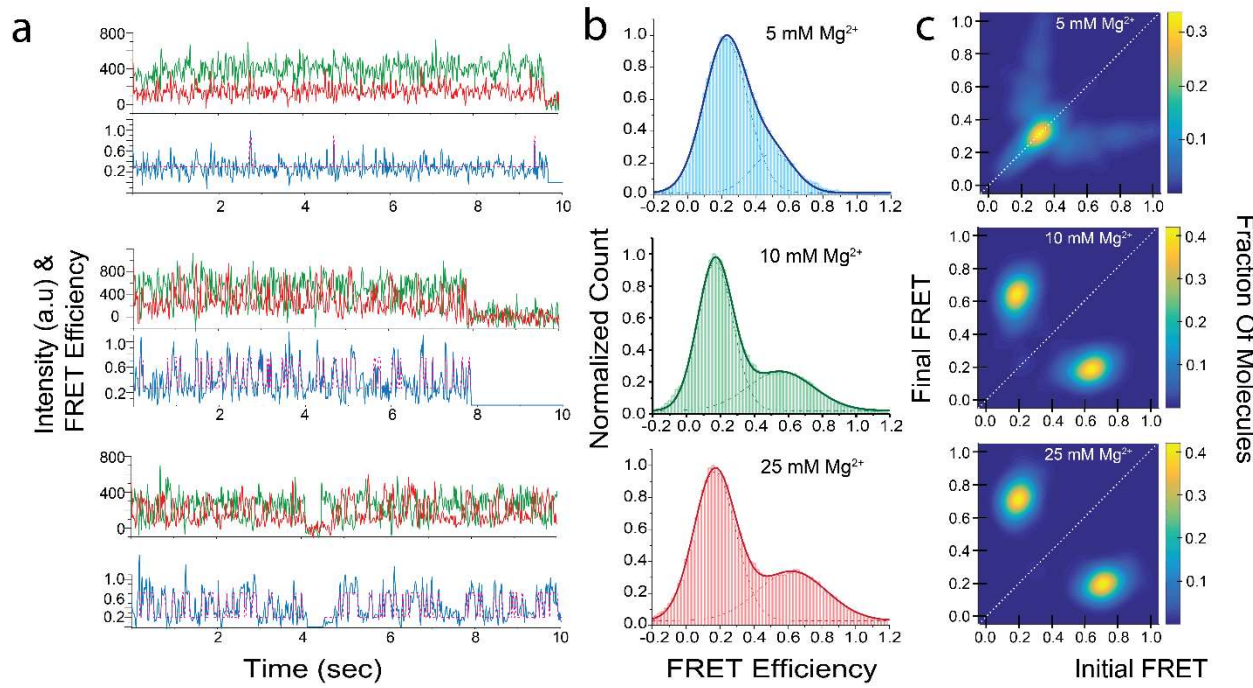
Supplementary Figures



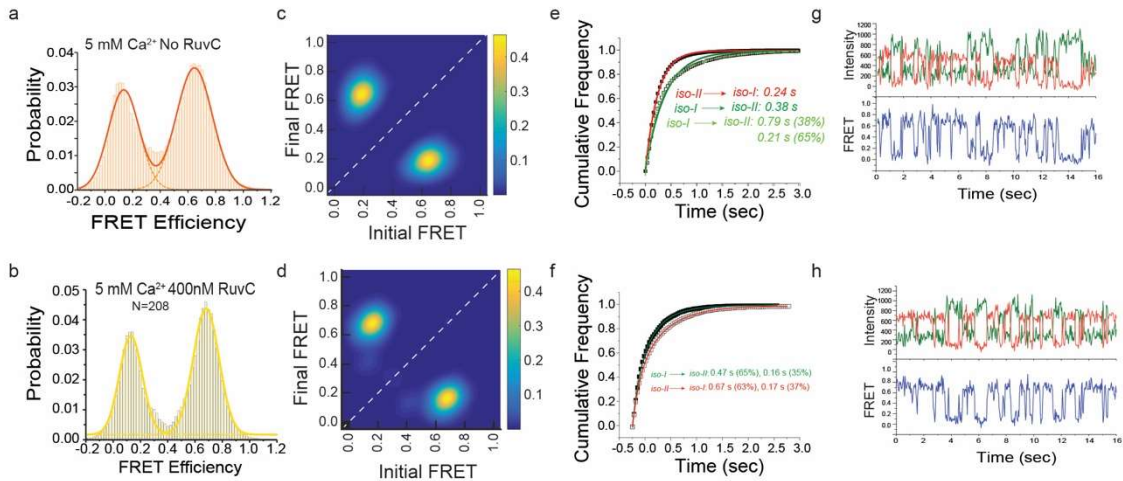
Supplementary Figure S1 | RuvC mediated Holliday Junction (HJ) resolution. **a** Schematic of the pathway in *E. coli* homologous recombination (HR). Formation and resolution of a Holliday junction (HJ) are highlighted; arrows indicate possible cleavage events. **b** Structure of RuvC in complex with Holliday junction substrate (adapted from PDB ID-4LD0, Gorecka *et. al.*(1)).



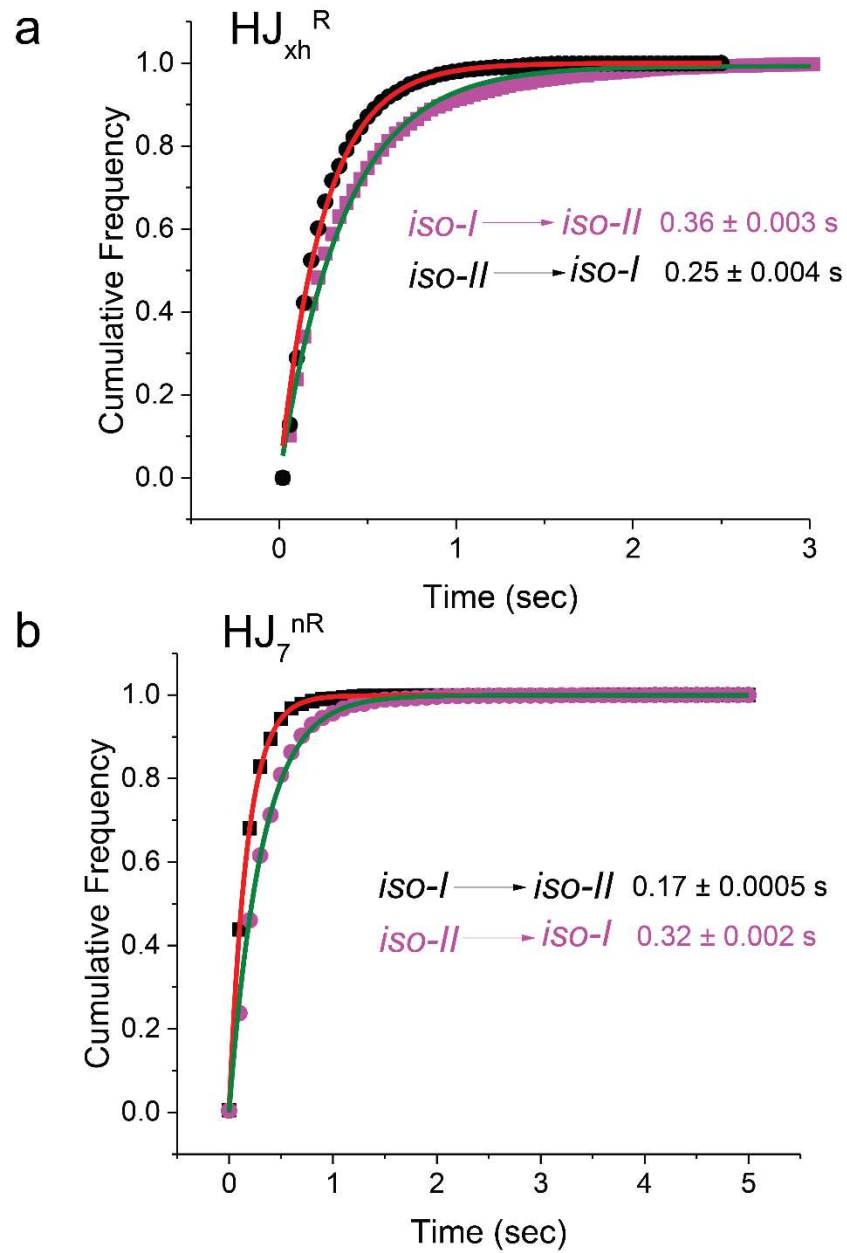
Supplementary Figure S2 | Steady-state equilibrium of doubly labeled $\text{HJ}_{\text{xh}}^{\text{R}}$ Holliday junction in the presence of Mg^{2+} ions. **a** Representative smFRET traces of conformational dynamics of $\text{HJ}_{\text{xh}}^{\text{R}}$ in the presence of 5 mM (upper panel), 10 mM (middle panel) and 25 mM (lower panel) Mg^{2+} . Green, Cy3 intensity; red, Cy5 intensity; blue, FRET efficiency; pink, HMM (Hidden Markov Model) idealization. **b** FRET efficiency histogram generated from the FRET efficiency traces at 5 mM (upper panel), 10 mM (middle panel) and 25 mM (lower panel) Mg^{2+} and fitted with a multi-peak Gaussian function. **c** Transition Occupancy Density Plots (TODPs) showing the fraction of HJs that undergo conformational transitions from a given initial FRET state to a given final FRET state at 5 mM (upper panel), 10 mM (middle panel) and 25 mM (lower panel) Mg^{2+} .



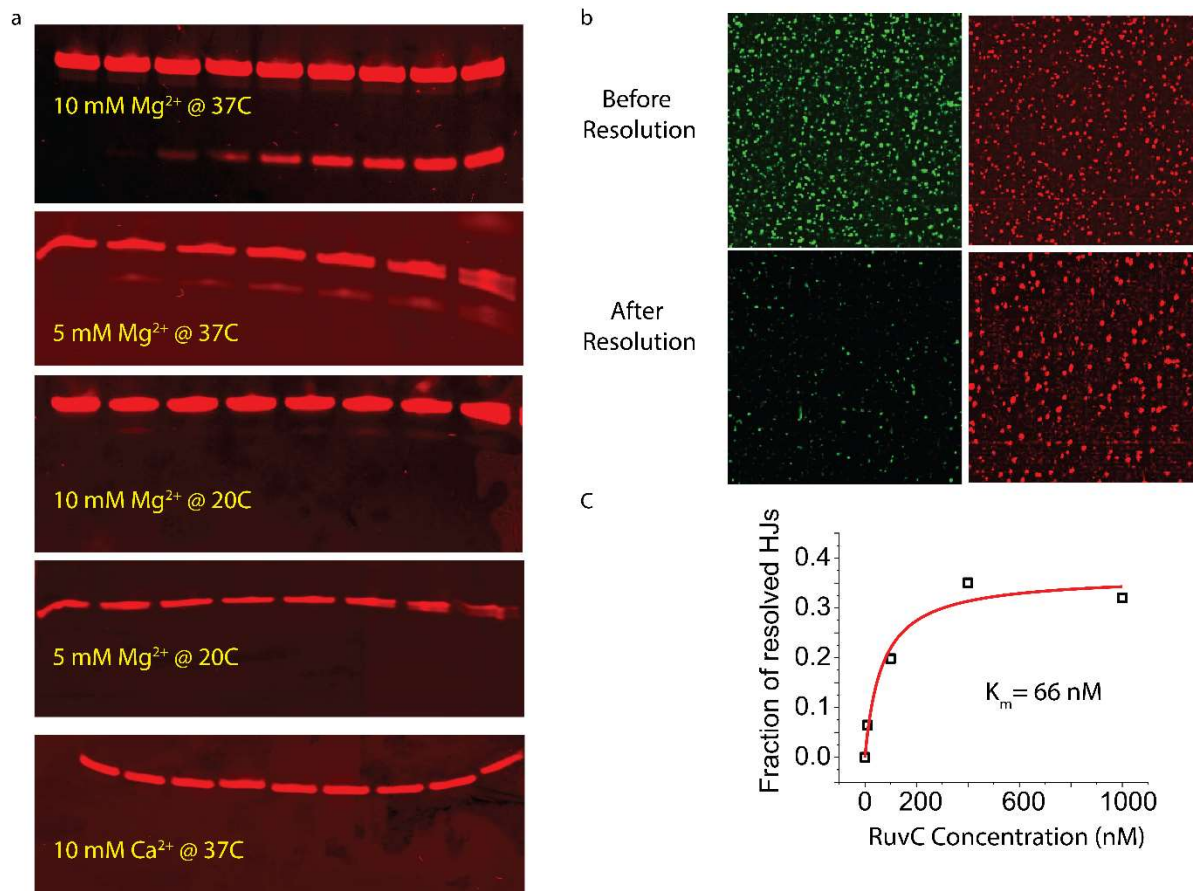
Supplementary Figure S3 | Steady-state equilibrium of dual labeled HJ₃ Holliday junction in the presence of Mg²⁺ ions. **a** Representative smFRET traces of conformational dynamics of HJ₃ in the presence of 5 mM (upper panel), 10 mM (middle panel) and 25 mM (lower panel) Mg²⁺. Green, Cy3 intensity; red, Cy5 intensity; blue, FRET efficiency; pink, HMM (Hidden Markov Model) idealization. **b** FRET efficiency histogram generated from the FRET efficiency traces at 5 mM (upper panel), 10 mM (middle panel) and 25 mM (lower panel) Mg²⁺ and fitted with a multi-peak Gaussian function. **c** TODPs showing the fraction of HJs that undergo conformational transitions from a given initial FRET state to a given final FRET state at 5 mM (upper panel), 10 mM (middle panel) and 25 mM (lower panel) Mg²⁺.



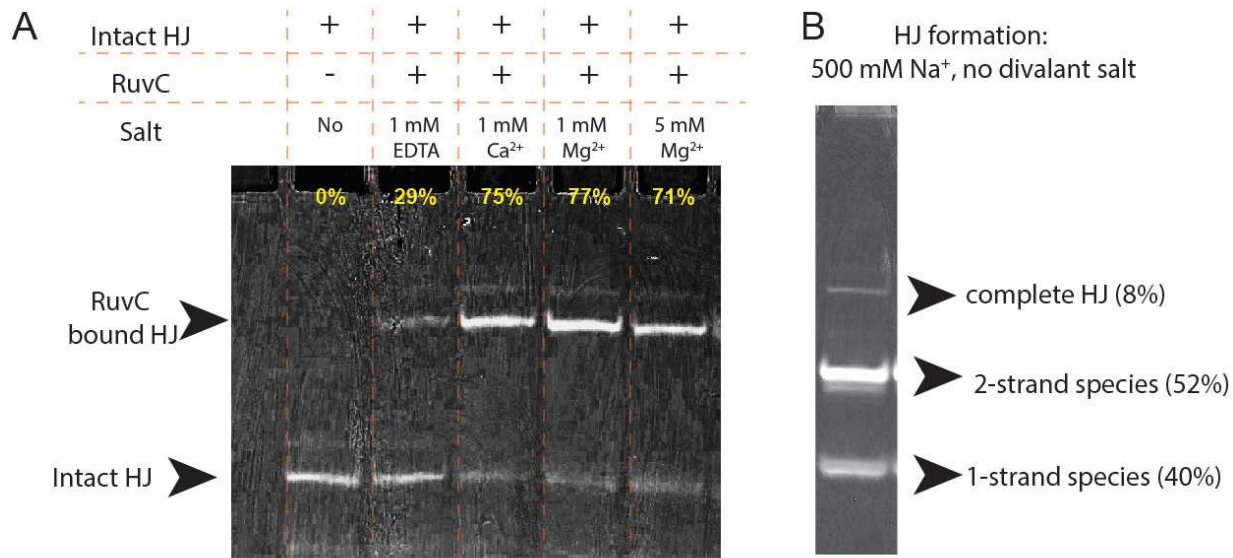
Supplementary Figure S4 | Steady-state equilibrium of dual labeled HJ_{xh}^R Holliday junction in the presence of Ca²⁺ ions. **a,b** FRET efficiency histogram generated from the FRET efficiency traces and fitted with a multi-peak Gaussian function in **a** 5 mM Ca²⁺ and **b** 5 mM Ca²⁺ and 400 nM RuvC. **c,d** TODP showing the fraction of HJs that undergo conformational transitions from a given initial FRET state to a given final FRET state in **c** 5 mM Ca²⁺ and **d** 5 mM Ca²⁺ and 400 nM RuvC. **e** Cumulative transition time curves for conformational dynamics of HJ_{xh}^R in 5 mM Ca²⁺; to the *iso*-I → *iso*-II transition, both single (dark green, adjusted R-square value: 0.988) and double (light green, adjusted R-square value: 0.999) exponential functions were fit, with the similar adjusted R-squared values suggesting that the single exponential value is reasonable to use. **f** Cumulative transition time curves for conformational dynamics of HJ_{xh}^R in 5 mM Ca²⁺ and 400 nM RuvC. **g,h** Representative single molecule traces in **g** 5 mM Ca²⁺ and **h** 5 mM Ca²⁺ and 400 nM RuvC.



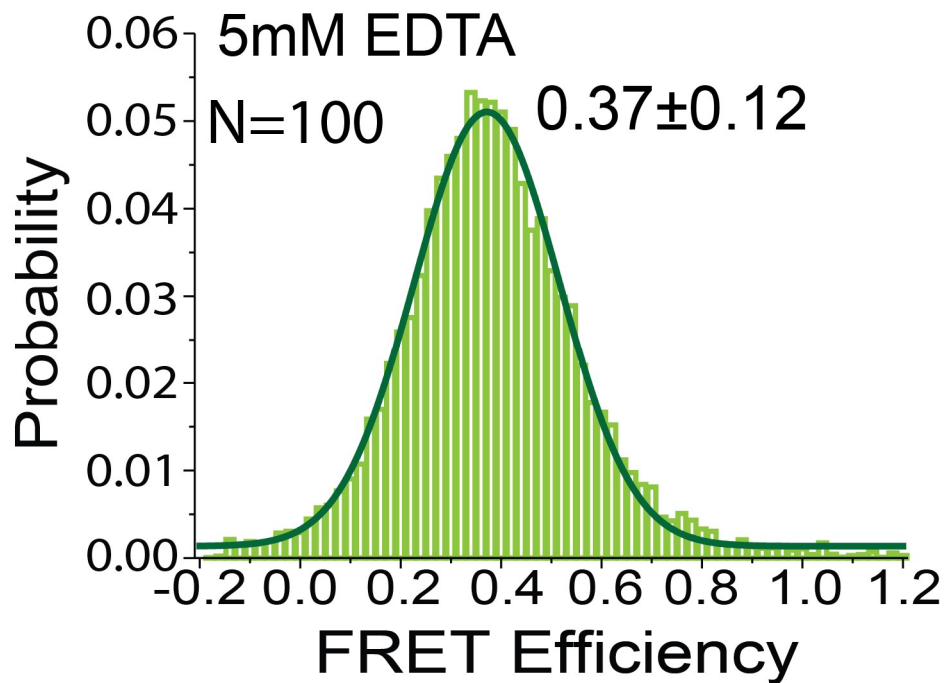
Supplementary Figure S5 | Cumulative dwell time plots and respective single exponential fits to extract the indicated conformational exchange rate constants for (a) $\text{HJ}_{\text{xh}}^{\text{R}}$ and (b) HJ_7^{nR} .



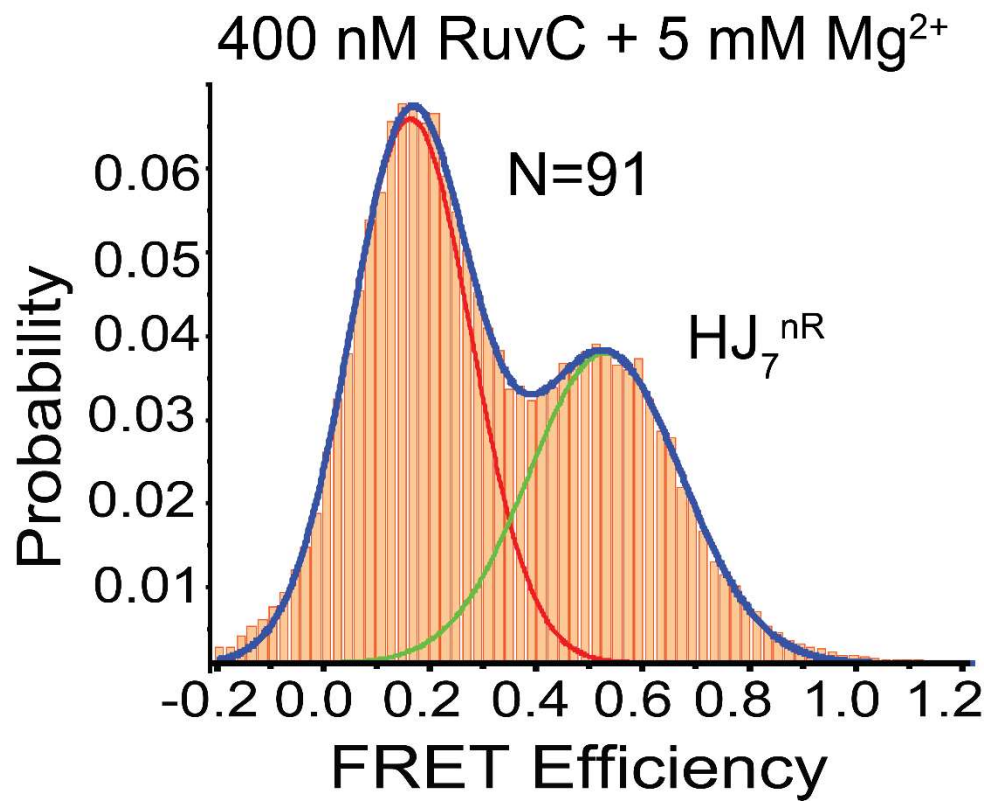
Supplementary Figure S6 | RuvC mediated cleavage assay for HJ_{xh}^R. **a** Denaturing Gels of RuvC mediated cleavage under different experimental conditions. The top band represents the uncleaved fraction whereas the lower band represents the cleaved fractions. **b** Camera images of single HJ molecules showing donor (green) and acceptor (red) channels before and after HJ resolution. The number of green molecules decreases significantly with cleavage. **c** Quantitative analysis of the RuvC mediated cleavage isotherm of HJs in the presence of 10 mM Mg²⁺ at 37 °C. RuvC was titrated (0 nM, 50 nM, 100 nM, 400 nM and 1000 nM) and the cleavage fraction calculated as the ratio of band intensity of the cleaved and uncleaved fractions (black squares). The data were fitted with a Michaelis-Menten equation (red line) to find a RuvC_{1/2} of 66 nM.



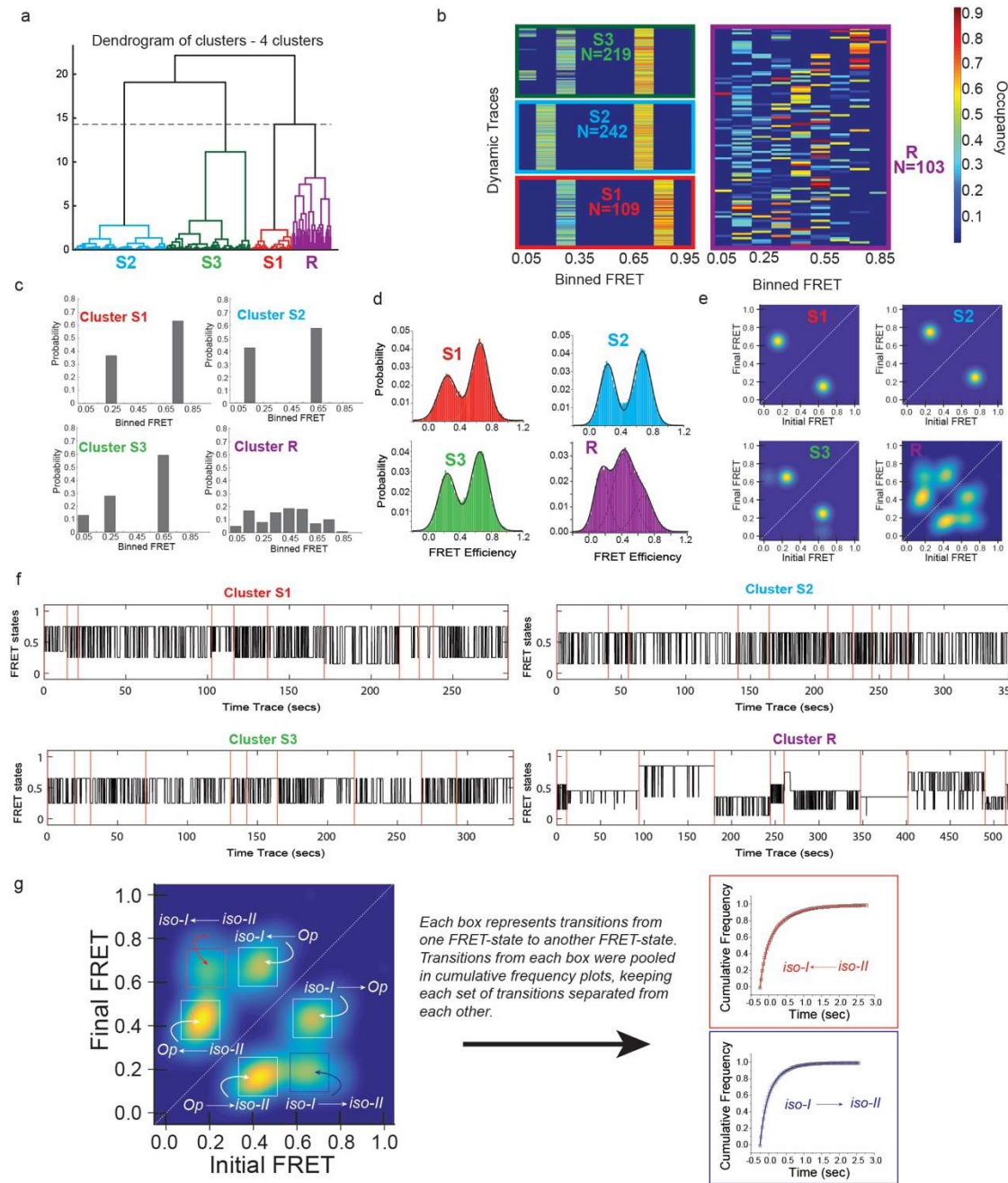
Supplementary Figure S7 | Native gel-based assay to study intact HJ formation and HJ-RuvC complex formation. **a** Assay of RuvC binding to HJ_{xh}^R under different buffer incubation conditions. The numbers on each lane represents percentage of HJs that are bound by RuvC. **b** Intact HJ_{xh}^R and different smaller fragments formation during the annealing process. Numbers in the parenthesis represents fraction of each complex. The gels were run at 12 W power at 4 °C in 1x TAE buffer (with a 1x gel loading buffer of 20% Glycerol, 0.005% (w/v) Bromophenol Blue, and the specified amount of salt in 1X TAE buffer).



Supplementary Figure S8 | smFRET histogram of HJ_{xh}^R in the absence of any divalent counter ions, representative of the Op state.

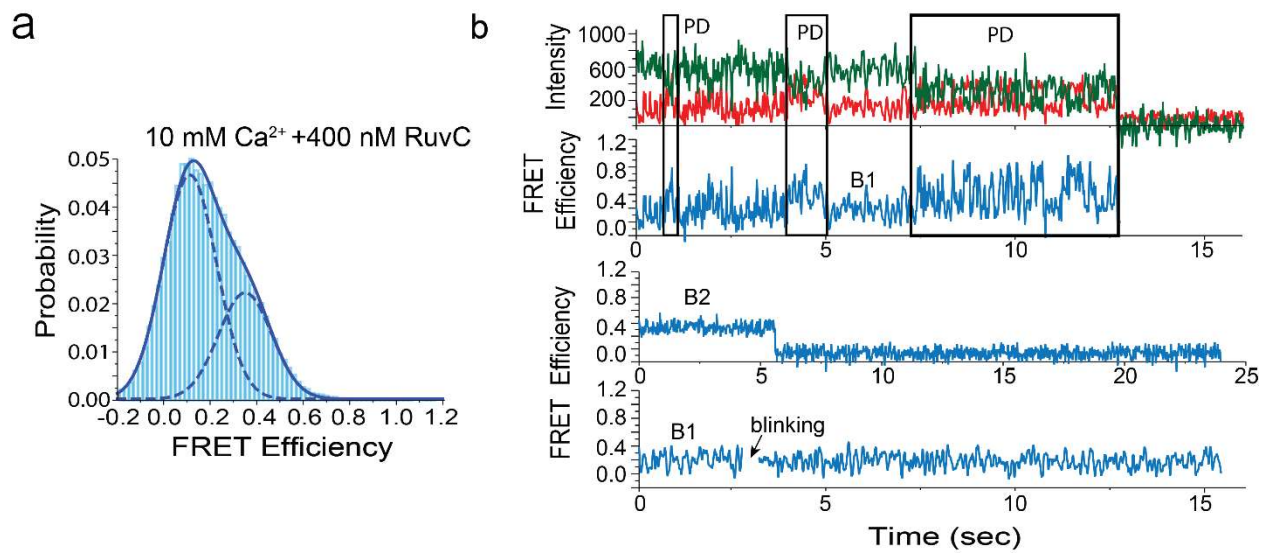


Supplementary Figure S9 | smFRET histogram for the HJ₇^{nR} construct in the presence of 5mM Mg²⁺ and 400 nM RuvC. No significant Op state is found.

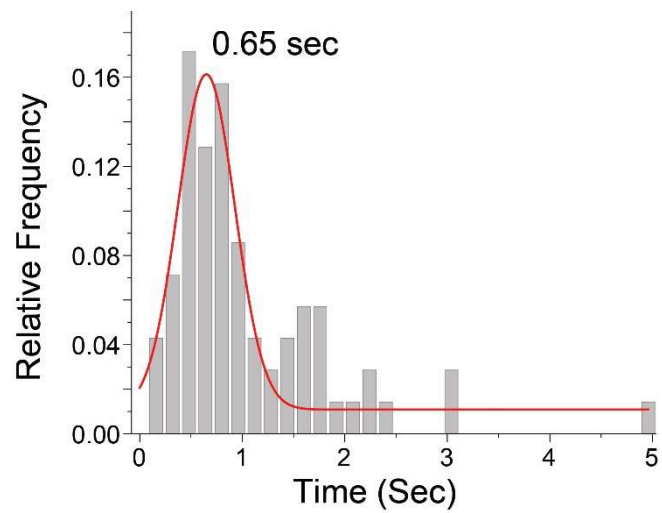


Supplementary Figure S10 | Single Molecule Cluster Analysis (SiMCAn) identifies classes of dynamic behaviors under different reaction conditions. a Dendrogram of dynamic traces resulting from hierarchical clustering analysis to identify patterns of trace behavior from 673 total molecules included in the analysis for HJ_{xh}^R. The dashed line indicates the threshold of 4 clusters used to describe the data. Dynamic clusters were assigned labels loosely based on the predominant properties of the cluster: S1 (red), S2 (cyan), S3 (green) represents buffer-only behavior and R (purple) represents RuvC-HJ complex behavior. **b** Occupancy heat maps for traces in each of the dynamic clusters shown in a. Each trace is represented by a single row in the heat map, and is colored according to the fraction of the

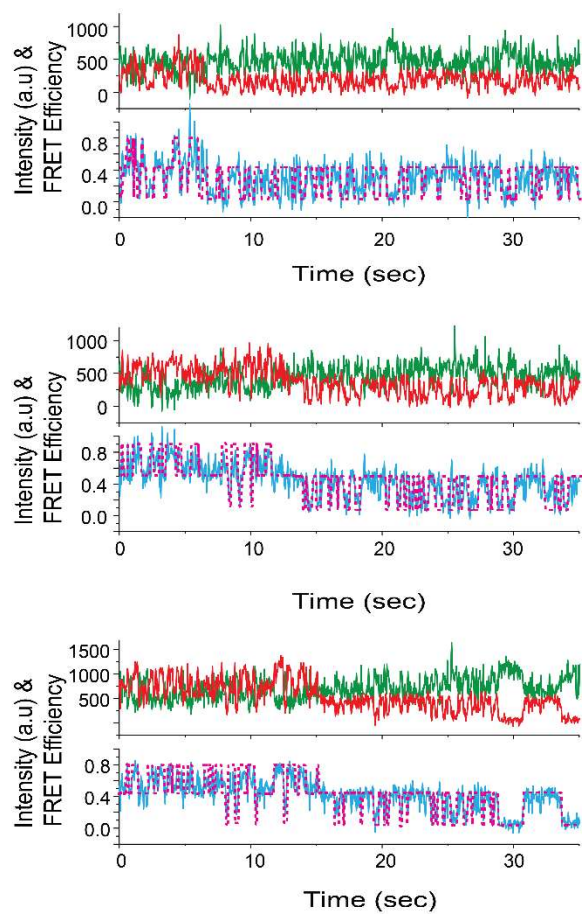
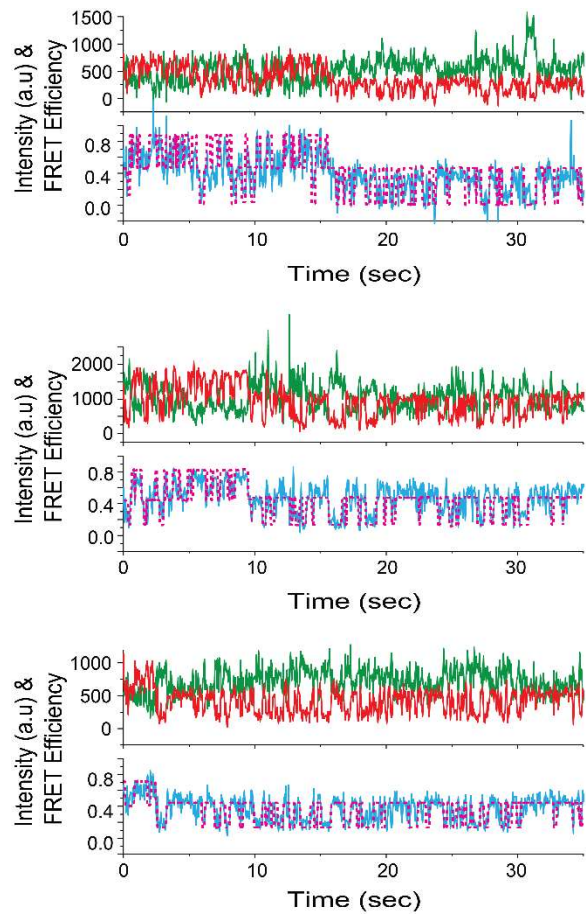
total observation time spent in each of the 10 binned FRET states (Occupancy). N, number of single molecule traces in the cluster. **c** Binned FRET efficiency histogram of all different clusters. Cluster S1, S2 and S3 mostly show two-state behavior, while cluster R shows the existence of multiple distinct states. **d** FRET efficiency histogram generated from the molecules belonging to each cluster. Multi-Gaussian fitting resulted in only two FRET peaks for cluster S1, S2 and S3 and three peaks for cluster R. **e** TODP generated from molecules belonging to different clusters. While S1, S2, S3 cluster molecules showed two-state kinetics, R-cluster molecules showed more distinct states. **f**. Each representation shows hundreds of seconds of several random (black) traces from each corresponding cluster. Clearly, S1, S2 and S3 cluster traces differ only by their FRET values, while the R-cluster shows very distinct states and state dynamics. **g**. To calculate transition rate constants between distinguished states, all dwell times in a particular FRET state were extracted across trajectories contributing to that population in the TODP by pooling transition times from user specified regions (shown by square box boxes). Example of the resulting cumulative frequency plots are shown on the right for the red and the blue boxes. This analysis separates the dwell times of different pathways based on the specific initial and the final FRET states visited.



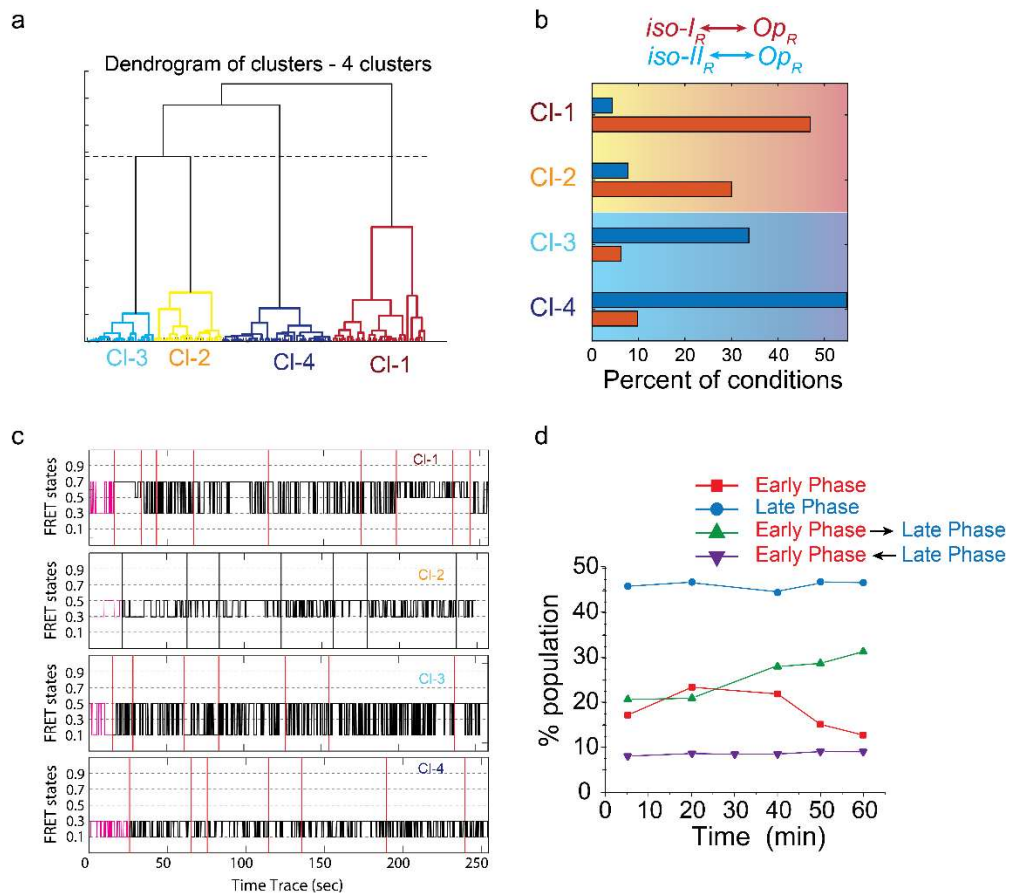
Supplementary Figure S11 | PD traces for HJ₇^{nR}. **a** FRET efficiency histogram of HJ₇^{nR}, with RuvC bound. RuvC was first bound at 1 mM Ca²⁺, followed by a buffer wash of 10 mM Ca²⁺. **b** smFRET time traces of RuvC-bound HJ₇^{nR} with different types of PD transitions, and bound B1 and B2 states.



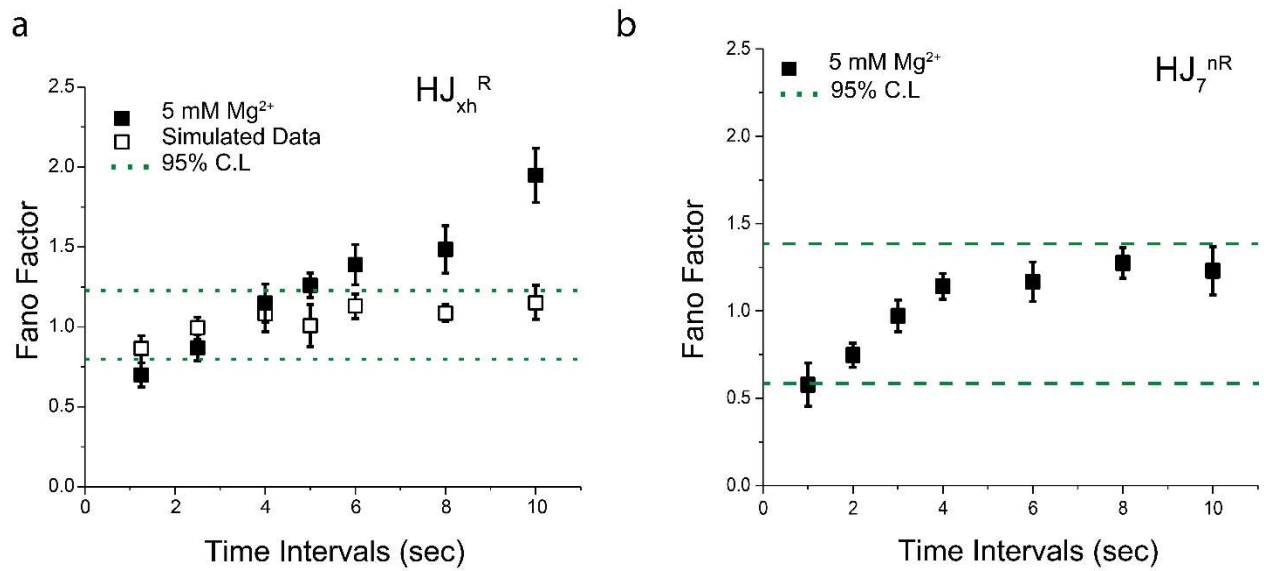
Supplementary Figure S12 | Duration of PD state analysis Relative frequency plot of the duration of PD state in the early phase. Single gaussian fit of the data provides an average time of 0.65 sec.



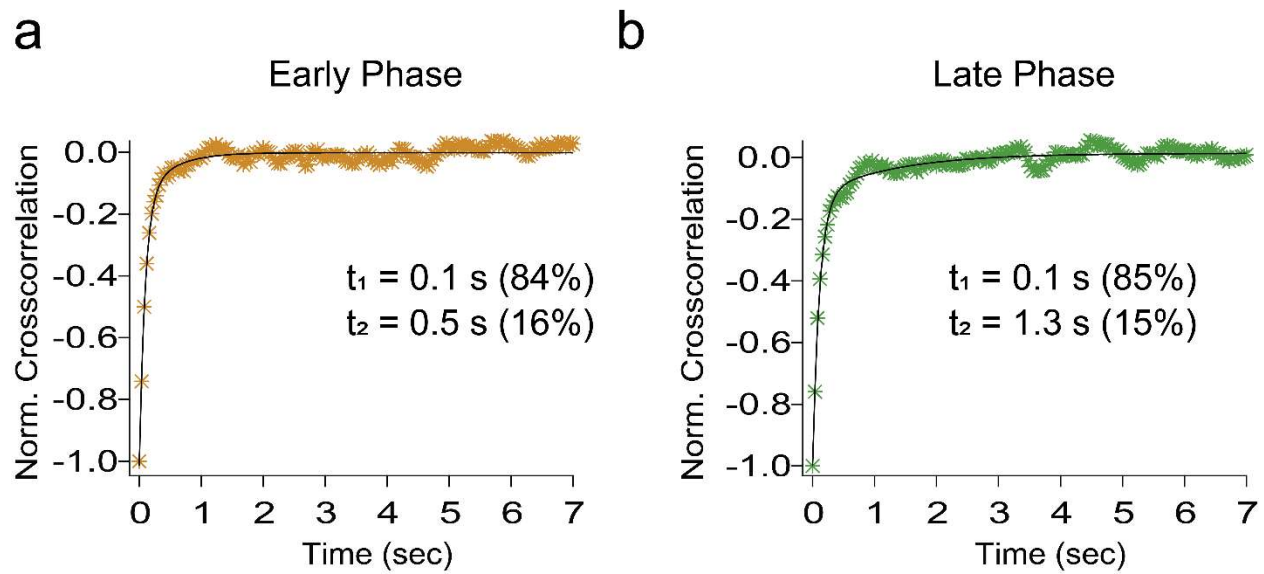
Supplementary Figure S13 | Representative smFRET time traces of the R cluster. The green plot represents the donor intensity, red plot represents the acceptor intensity, the blue plot represents the FRET efficiency and the magenta represents HMM fitting of the smFRET data over time.



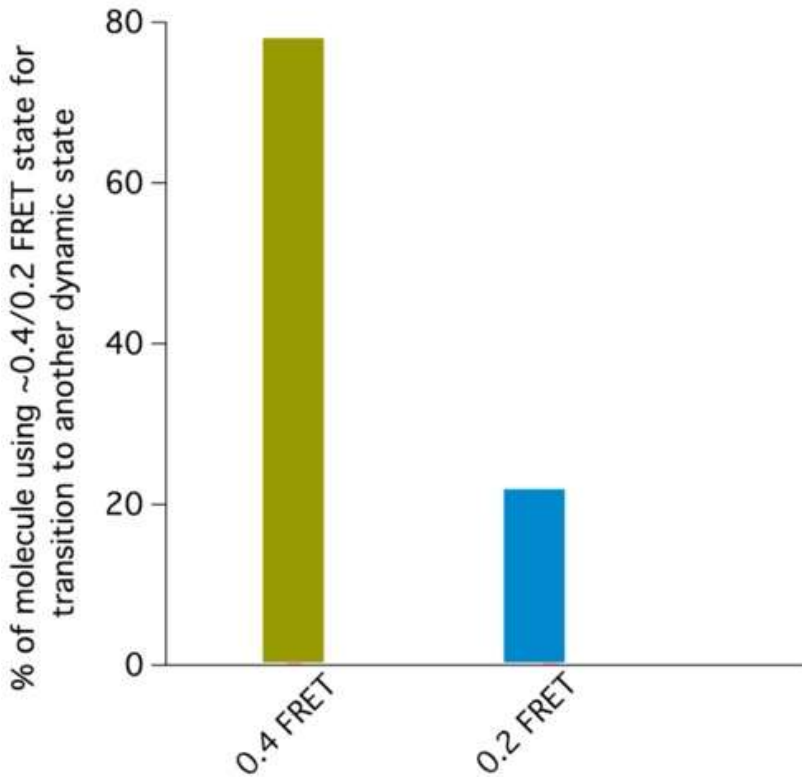
Supplementary Figure S14 | Second layer of clustering and time evolution of different transition behaviors. **a** Dendrogram of dynamic traces resulting from hierarchical clustering analysis to identify patterns of trace behavior from 57 total molecules included in the analysis. The dashed line indicates the threshold of 4 clusters used to describe the data. Dynamic clusters were assigned labels loosely based on the predominant properties of the cluster: CI-1 (red), CI-2 (yellow), CI-3 (cyan) and CI-4 (blue). **b** Summary of a second level of SiMCAn results, showing bar graphs with occupancy of the four clusters found in early and late phases of the transition traces. Clusters CI1, CI2 consists of the mostly early phases of the transition traces (orange bar), representative of the $iso-I_R \leftrightarrow Op_R$ behavior while CI-3 and CI-4 consists of mostly late phases of the traces (blue bar), representative of the $iso-II_R \leftrightarrow Op_R$ behavior. **c** Representative traces from each cluster. The trace closest to the cluster center (magenta), up to 250 s of random (black) traces from the cluster. Each red vertical line demarcates individual trajectories. **d** Time evolution of different nature of traces found in the R cluster. Traces with constant $iso-I_R \leftrightarrow Op_R$ (red square), constant $iso-II_R \leftrightarrow Op_R$ (blue circle), transition from $iso-I_R \leftrightarrow Op_R$ to $iso-II_R \leftrightarrow Op_R$ (green up triangle) and vice versa (purple down triangle) over time. 77% of molecules are in the late phase after an hour of incubation with RuvC in 5 mM Mg²⁺ where they are primed to be cleaved, whereas ~12% of molecules remain in the early phase and 10% molecules go back and forth between the early and late phases.



Supplementary Figure S15 | Fano factor calculation for the HJ_{xh}^R and HJ₇^{nR} Holliday junctions in the presence of 5 mM Mg²⁺ ions. The Fano factor was calculated across various time intervals for the 5 mM Mg²⁺ dataset (solid squares). The Fano factor for a simulated dataset with the same overall rate constant, trace length and trace number, but derived from a purely Poisson distribution was also calculated and plotted (open squares). The dashed lines indicate the 95% confidence intervals for a Poisson-like process with a specific number of trajectories. The Fano factor values for the 5 mM Mg²⁺ dataset deviate from 1, indicating an underlying non-random distribution with multiple repetitive processes, while the simulated Poisson data remain close to 1.



Supplementary Figure S16 | Cross correlation analysis. **a** Normalized cross correlation as a function of time for early phase shows double-exponential behavior with two time constants of 0.1 s and 0.5 s. **b** Normalized cross correlation as a function of time for late phase shows double-exponential behavior with two time-constants of 0.1 s and 1.3 s.



Supplementary Figure S17 | Percentage of molecules going through an Op state as an intermediate step to another dynamic state. Bar graphs showing the percentage of molecules displaying $E_{FRET} = 0.4$ and $E_{FRET} = 0.2$ as intermediate states before transitioning into another dynamic state. The mid-FRET value of 0.4 (corresponding to the Op state) is observed in ~78% of molecules as a transitory state whereas only ~20% of molecules transition through $E_{FRET} = 0.2$ into another dynamic state. This makes the Op state ($E_{FRET} = 0.4$) a near-obligatory intermediate between two distinct FRET states (i.e., *iso-I* and *iso-II*).

Supplementary Reference

1. Gorecka, K.M., Komorowska, W. and Nowotny, M. (2013) Crystal structure of RuvC resolvase in complex with Holliday junction substrate. *Nucleic Acids Res*, **41**, 9945-9955.